Journal of Computational Physics 424 (2021) 109836

Contents lists available at ScienceDirect

Journal of Computational Physics

www.elsevier.com/locate/jcp

A computational model applied to myocardial perfusion in the human heart: From large coronaries to microvasculature

Simone Di Gregorio [a], Marco Fedele [a], Gianluca Pontone [b], Antonio F. Corno [c], Paolo Zunino [a], Christian Vergara [d,*], Alfio Quarteroni [a,e]

[a] MOX, Dipartimento di Matematica, Politecnico di Milano, Italy
[b] Centro Cardiologico Monzino IRCSS, Milan, Italy
[c] Houston Children's Heart Institute, Hermann Children's Hospital, University Texas Health, McGovern Medical School, Houston, TX, USA
[d] LABS, Dipartimento di Chimica, Materiali e Ingegneria Chimica "Giulio Natta", Politecnico di Milano, Italy
[e] Institute of Mathematics, École Polytechnique Fédérale de Lausanne, Switzerland

ARTICLE INFO

Article history:
Received 28 November 2019
Received in revised form 27 August 2020
Accepted 3 September 2020
Available online 18 September 2020

Keywords:
Cardiac perfusion
Multi-compartment Darcy model
Intramural vessel network
Iterative numerical scheme
Finite elements
Perfusion regions

ABSTRACT

In this paper we present a mathematical and numerical model for human cardiac perfusion which accounts for the different length scales of the vessels in the coronary tree. Epicardial vessels are represented with fully three-dimensional (3D) fluid-dynamics, whereas intramural vessels are modeled as a multi-compartment porous medium. The coupling of these models takes place through interface conditions based on the continuity of mass and momentum. Instead, is neglected in this first preliminary model the myocardium deformation. To estimate the physical parameters of the multi-compartment model, a virtual intramural vascular network is generated using a novel algorithm which works in non-convex domains. Modeling epicardial vessels with a 3D model and intramural ones with a porous medium approach makes it possible to apply the proposed strategy to patient-specific heart geometries reconstructed from clinical imaging data. We also address the derivation of numerical solvers for the coupled problem. In particular, we propose a splitting algorithm for the monolithic problem, with the corresponding convergence analysis performed in a simplified linearized case, and a suitable preconditioner for the multi-compartment porous sub-model. Finally, we test the computational framework in a realistic human heart, obtaining results that fall in the physiological range for both pressures and local myocardial flows.

© 2020 Elsevier Inc. All rights reserved.

1. Introduction

The cardiac muscular tissue (myocardium) requires continuous oxygen supply to properly work, i.e. to contract and pump the blood into the whole arterial system. Oxygenated blood reaches the heart through the coronaries and perfuses the whole myocardium, allowing the exchange of oxygen at the level of the microvasculature [66]. A reduced oxygen delivery to the myocardium can occur in the presence of flow reduction either because of the presence of coronary arteries obstructions, like in atherosclerosis, as well as in the presence of normal coronary arteries because of a severe aortic valve regurgitation,

* Corresponding author.
E-mail addresses: simone.digregorio@polimi.it (S. Di Gregorio), marco.fedele@polimi.it (M. Fedele), gianluca.pontone@cardiologicomonzino.it (G. Pontone), antonio.f.corno@uth.tmc.edu (A.F. Corno), paolo.zunino@polimi.it (P. Zunino), christian.vergara@polimi.it (C. Vergara), alfio.quarteroni@polimi.it (A. Quarteroni).

https://doi.org/10.1016/j.jcp.2020.109836
0021-9991/© 2020 Elsevier Inc. All rights reserved.

with steal of coronary flow during diastole, or because of severe left ventricular hypertrophy, causing inadequate oxygen delivery, like in severe aortic valve stenosis or chronic systemic hypertension.

The direct measurement of blood perfusion is nowadays possible by means of *myocardial blood flow* (MBF) maps [45,12, 51] or *myocardial perfusion reserve* [68,17,6], obtained by Computed Tomography (CT) scan and Magnetic Resonance Imaging (MRI), respectively. However, these techniques are still seldom used in the daily diagnostic practice, also because they require very expensive procedures, which are also very demanding for the patients in terms of radiological exposition and/or duration of the acquisition exam. In addition, we have to take in account that a realistic coronary tree reconstruction should provide not only morphometric data but also information about the flow [49]. The myocardium is the organ in the body with the highest oxygen consumption and extraction per gram [29], and the coronary blood flow is controlled by multiple mechanisms [29,49], with the coronary microvessels responsible for the major portion of the flow resistance [49].

Numerical simulation can in principle provide meaningful quantitative information about myocardial perfusion, both in physiological and in pathological conditions. It allows, for instance, to quantify the amount of blood perfusing the different regions of the myocardium for selected virtual scenarios of coronary artery stenosis. For this reason several authors have developed in the past few years mathematical and numerical models for a better understanding of such process.

For a comprehensive mathematical description of myocardial perfusion, we detail in what follows the specific processes and features that should be considered in the models, together with some related significant works.

1. The coronary tree is characterized by the co-existence of multiple space scales, going from the large coronaries (~ 1 mm), to the arterioles and venules (~ 0.1 mm), until the microvasculature (~ 0.01 mm) [43]. Since only the large coronaries are detectable by the standard imaging techniques, it is mandatory to properly build surrogate models for arterioles/venules and microvasculature or reconstruct them from *ex-vivo* data. The blood dynamics in the largest coronaries is typically described by means of the 3D fluid-structure interaction problem [30,37], the 3D Navier-Stokes equations in rigid domains [61,60], or the reduced 1D model for blood flow [64]. Regarding the modeling of the medium and micro- vasculature, a multi-compartment model based on a hierarchical subdivision of the vessels has been considered in [33,32]. After operating an homogenization procedure, the blood flow in the myocardium is treated as the flow through a porous medium. In this respect, a straight Darcy model has been considered in [42], whereas a more-sophisticated multi-compartment Darcy model has been proposed in [15,47,34,35,41], see also [57] for an application to the perfusion in the liver.
2. The interaction between the cardiac muscle and the coronaries is relevant because there is a strong interplay between the blood dynamics in the large vessels, which are usually located on the epicardium, and that in the medium and micro- vessels which sit in the myocardial muscle. Indeed, pressures and flow rates are continuously exchanged. With this aim, a 1D-3D model for the coupling between large coronary arteries and intramural vessels has been considered in [47,35,42,41].
   Further, the coronary flow rate is strongly influenced by the cardiac muscle contraction. During the systolic phase the myocardial contraction increases the ventricular pressure, causing the compression and the closure of the intramural coronary vessels. The corresponding increase of vascular resistances leads to a decrease of the coronary blood flow during the systole. On the contrary, during the diastolic phase, the myocardial relaxation reduces the ventricular pressure, the lumen of the intramural coronaries is open and the tissue can be widely perfused [77]. This effect is usually called the systolic inhibition. To account for this, some authors considered a poro-elastic model of the myocardium, see e.g. [33,13,15,42,41,75].
3. Selective perfusion is important because recent studies suggested that the myocardium is composed by well defined regions which are perfused by distinct arterial coronaries [67]. For the modeling of such feature, a subdivision of the myocardium in perfusion regions has been proposed in [15], see also [9] for an application to the upper limb.
4. A complete description of both ventricles is particularly relevant in view of an integrated model of myocardial perfusion and coronary hemodynamics, accounting for the blood supply provided by the coronary arteries, with the total coronary blood flow unequally distributed between right and left coronary arteries [6], and for the corresponding coronary venous return.

On the basis of the works reviewed above, we present a mathematical model applied to myocardial perfusion in both left and right ventricles of a human heart. We adopt a multi-physics approach where we couple the 3D blood dynamics inside the large coronary vessels with the blood dynamics inside the intramural vasculature, which is modeled by means of 3D multi-compartment Darcy equations. This model requires a set of parameters, the estimation of which depends on the topology of the network of the intramural vessels. To this purpose, we propose an algorithm to generate a surrogate intramural vascular network in a biventricular geometry combining the algorithm proposed for the cube in [34] with the strategy proposed in [63] for the generation of vessels in non-convex domains. This approach has the advantage to be directly applicable to data that are available in clinical practice, such as the CT scan of the coronary tree (also named CT angiography, CTA). In fact, such data allow to reconstruct the geometries of the main epicardial coronaries and the ventricles. Moreover, we carry out an in-depth investigation of the numerical approximation of the multi-physics coupled problem. In particular, we propose an iterative algorithm to split the monolithic problem and we provide a convergence analysis for a simplified linearized version of the problem. Further, we approximate the Navier-Stokes and the multi-compartment Darcy subproblems by means of backward differences formula for time and Finite Elements for space discretizations and we

propose a block diagonal preconditioner for the algebraic problem related to the multi-compartment Darcy problem. Finally, we assess the validity of the proposed algorithms by means of numerical experiments both in an ideal and in a realistic scenario, taking a first step towards the validation of the proposed models.

The outline of this work is as follows. In Section 2 we present the mathematical coupled problem, the strategy for the partition of the myocardium, and we describe how to generate the intramural network for the estimation of the multi-compartment Darcy model parameters. In Section 3 we introduce the Finite Elements and time discretizations, we detail the splitting strategies to handle the coupled problem and we describe the preconditioners used for the solution of the linear systems. In Section 4 we present several numerical results showing the effectiveness of the mathematical and numerical models proposed in this work. We conclude the paper with some final remarks in Section 5.

2. Multi-physics modeling of myocardial perfusion

The morphology of the coronary arterial tree (form large vessels to capillaries) has a well-defined structure, as illustrated in Fig. 1(a). The large coronaries start at the aortic root and spread along the epicardial surface. A clear scale separation is observed between the main vessels laying on the epicardium and the smaller vessels penetrating into the tissue. Following the subdivision proposed in [43], we name the former as *epicardial coronaries* and the latter as *intramural vessels*. We point out that in this classification we include microvessels and in particular capillaries into the intramural vessels. Intramural vessels should not be confused with the *intramural coronary artery*, which refers to the coronary patterns in which there is an intimate relationship between aortic and coronary arterial walls; histologically, the aortic and coronary medial walls are attached without interposed adventitia [48]. We also observe that much smaller vessels depart transversally from the main coronaries and penetrate into the cardiac muscle to perfuse portions of it. We refer to such vessels as *transversal vessels*.

On the basis of the observable scale separation, multiscale and multi-physics approaches seem the only viable choice for a comprehensive mathematical description of myocardial perfusion. In this work, we adopt a multi-physics model where epicardial vessels are represented as three-dimensional objects (see Sect. 2.1). To model the variation and the evolution of spatio-temporal fields, such as the pressure, in the intramural vessels, we adopt a homogenization approach leading to a multi-compartment porous medium model in the myocardium (see Sect. 2.2). This model is well suited to be coupled with the 3D description of the coronary flow because they share the same geometric dimension and mathematical structure. However, the coefficients characterizing such a model are difficult to measure, partly because they may vary in space through the myocardium. For this reason we introduce a (sub-scale) description of the myocardium into perfusion districts combined with the generation of virtual intramural vascular trees, respecting the fundamental physiological principles. Even if this subscale description could be used to obtain a direct accurate numerical solution (as an example the whole myocardium will be split in our case reported here into 17 perfusion regions each containing thousands of vessels), due to the computational effort we use them only to estimate the physical parameters characterizing the porous medium perfusion model, see Section 2.4. In conclusion, the proposed multi-physics model consists in the 3D description of blood flow coupled with a multi-compartment porous medium model applied to the myocardial perfusion. The coupling takes place at multiple levels: directly, through interface conditions based on the continuity of mass and of momentum (see Sect. 2.3), and indirectly, through the virtual network of intramural vessels. The design of the multi-physics model is displayed in Fig. 1.

2.1. Fluid-dynamics in the epicardial coronary vessels

Nowadays standard biomedical imaging acquisition techniques, like CT scan, allow to detect and reconstruct only the large coronaries, above 1 mm of diameter. For such vessels (usually up to about 20 vessels for the most detailed level of reconstruction), classical segmentation techniques [4] can be applied to reconstruct the 3D patient-specific vascular geometry. 3D Navier-Stokes (NS) equations are then used to model the blood dynamics therein. Although far more computationally expensive than 1D flow models (very often used for the coronary tree), 3D models ensure a better accuracy and a better fit of the patient coronary shapes. These features are of primary importance, e.g. to evaluate the vascular flow reserve, as well as to better capture flow disturbance downstream a stenosis, an instance that could have a great impact on the clinical applications of the cardiac perfusion model. Notice however that we are not accounting here for the compliance of the coronary vessels wall. Fluid-structure interaction problems, where 3D NS equations are coupled with suitable elastodynamic equations for wall deformation [55], possibly combined to poro-elasticity models for the intramural vessels, could provide an interesting improvement for future studies.

Referring to Fig. 2, the blood dynamics in the coronary domain Ω_C are modeled by means of the Navier-Stokes equations for an incompressible, homogeneous, and Newtonian fluid [54], under the assumption of rigid walls:

$$\rho\left(\frac{\partial \boldsymbol{u}_C}{\partial t} + (\boldsymbol{u}_C \cdot \nabla)\boldsymbol{u}_C\right) - \mu\nabla \cdot \left(\nabla \boldsymbol{u}_C + (\nabla \boldsymbol{u}_C)^T\right) + \nabla p_C = \boldsymbol{0} \qquad \text{in } \Omega_C, \tag{1a}$$

$$\nabla \cdot \boldsymbol{u}_C = 0 \qquad \text{in } \Omega_C,$$

$$\boldsymbol{u}_C = \boldsymbol{0} \qquad \text{on } \Gamma_w, \tag{1b}$$

$$\boldsymbol{u}_C = \boldsymbol{u}_{in} \qquad \text{on } \Gamma_{in}, \tag{1c}$$

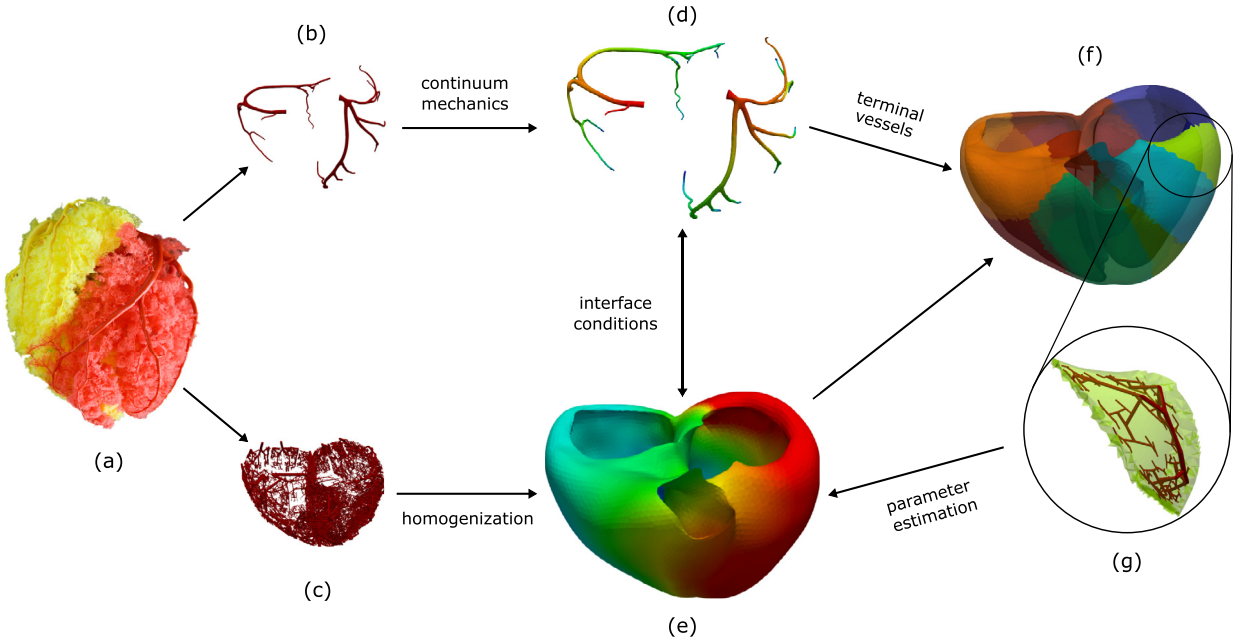


Fig. 1. (a) Cast of Coronary Arteries, source Wikipedia; (b) epicardial vessels; (c) intramural vessels; (d) 3D blood flow dynamics model inside coronary domain (pressure depicted); (e) porous media flow model inside myocardial domain (pressure depicted); (f) myocardium partitioned into different perfusion regions; (g) example of generated intramural vascular network inside a perfusion region.

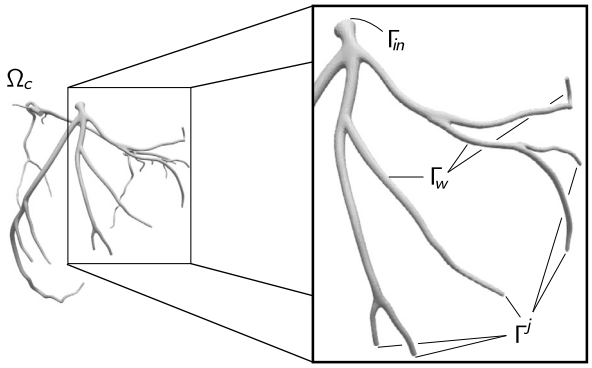


Fig. 2. Sketch of the computational domain for the epicardial coronary vessels.

where $\boldsymbol{u}_C$ and p_C are the blood velocity and pressure, respectively, in the epicardial coronaries, ρ the blood density, μ the blood viscosity; Γ_w is the lateral physical vessel wall, where a no-slip condition (1b) is prescribed. The surface Γ_w includes also the outlet sections feeding the atria, where we assume that the flow rate is negligible with respect to the ventricular outlets [71]; Γ_{in} is the inlet section representing the coronary left and right ostia located at the aortic root, where a physiological velocity profile $\boldsymbol{u}_{in}$ is imposed.

As we can notice from Fig. 2, the computational domain is composed also by the distal outflow sections Γ^j, $j = 1, \ldots, J$. Here, the coupling with the intramural vasculature is considered. The corresponding coupling interface conditions will be discussed in Sect. 2.3.

2.2. Fluid-dynamics in the intramural vasculature: multi-compartment Darcy model

In this section we introduce a mathematical model for the intramural (medium and micro) vessels. We consider a porous media model for the description of the myocardium because the standard biomedical *in-vivo* imaging techniques do not allow to reconstruct the patient-specific geometry of the intramural vasculature. To account for the different length scales of the vessels in such a region, we consider a 3D multi-compartment Darcy model [34,35]. That requires the introduction of parameters representing the local permeability and conductance among compartments.

The multi-compartment Darcy model relies on using the Darcy equation in every compartment, featuring different length scales, that coexist in the same domain Ω_M representing the myocardial muscle [34,35,47,15]. The equations of Darcy flow for compartment $i \in [1, N]$, with N being the number of compartments, are:

$$\boldsymbol{K}_i^{-1}\boldsymbol{u}_{M,i} + \nabla p_{M,i} = \boldsymbol{0} \qquad \text{in } \Omega_M, \tag{2a}$$

$$\nabla \cdot \boldsymbol{u}_{M,i} = g_i - \sum_{k=1}^{N} \beta_{i,k}(p_{M,i} - p_{M,k}) \qquad \text{in } \Omega_M, \tag{2b}$$

$$\boldsymbol{u}_{M,i} \cdot \boldsymbol{n} = 0 \qquad \text{on } \partial\Omega_M, \tag{2c}$$

where, in the i-th compartment for $i = 1 \dots N$, $\boldsymbol{u}_{M,i}$ and $p_{M,i}$ are the Darcy velocity and the pore pressure, respectively, $\boldsymbol{K}_i$ the permeability tensor, g_i a volumetric source (or sink) term, and $\beta_{i,k} \geq 0$, $i, k = 1 \dots N$, represent the inter-compartment pressure-coupling coefficients. In particular, the model hypothesizes that due to mass conservation, the divergence of the Darcy velocity is compensated by a source or sink external term and by mass exchanges between different compartments, which depend on the pressure jumps between the latter. To enforce mass conservation among compartments, we have that $\beta_{i,k} = \beta_{k,i}$, $\forall i, k = 1, \dots, N$. Moreover, $\beta_{i,k} \neq 0$ whenever $k = i \pm 1$ for $2 \leq i \leq N-1$, $k = 2$ for $i = 1$, $k = N-1$ for $i = N$, since the compartment i exchanges mass only with adjacent compartments. The estimation of such parameters will be investigated in Sect. 2.4.

The first compartment is the one upstream, its g_1 will be provided by the epicardial blood dynamics (see Sec. 2.3). Instead, the volumetric term of the farthest away compartment g_N (i.e. the microvasculature), is a sink term that accounts for coronary venous return, see Section 2.3. Finally, we notice that $g_j = 0$, $j = 2, \dots, N-1$, since the intermediate compartments do not exchange mass with the external environment.

From the mass conservation and the null flux conditions on the epicardial and endocardial surface $\partial\Omega_M$ (2c), we have the following compatibility condition:

$$\int_{\Omega_M} (g_1 + g_N) d\boldsymbol{x} = 0.$$

For our purposes, we deem that three compartments are enough for a description of the hemodynamics in the intramural vessels, see also [35]. We will therefore set $N = 3$ from now on.

Notice that the most of the blood perfusion in the myocardium (about 80% [29]) occurs during the relaxation phase, when the deformation of the myocardial muscle does not affect significantly the intramural vessels cross-section. This motivates our choice to neglect, as a first approximation, the myocardial movement due to heart contraction and relaxation.

2.3. Mathematical formulation of the coupled problem and coupling conditions

In this section we close the mathematical problems introduced in the previous sections by providing the coupling conditions between the epicardial and the intramural hemodynamics. We need two coupling conditions, one ensuring the conservation of mass and another one for the balance of interface forces (third Newton law, see [56]).

We also identify *perfusion regions* Ω_M^j, $j = 1, \dots, J$, [67] where the exchange of information between epicardial and intramural vessels occurs. We assume that there is a one-to-one correspondence between outlets of epicardial vessels and perfusion regions. So to have exactly J perfusion regions. The procedure used to partition the myocardial domain in non-overlapping perfusion regions will be described in Section 2.4.1. The coupling conditions between NS equations (1a)-(1c) and the multi-compartment Darcy model (2a)-(2c) are the following:

a) conservation of mass: the first compartment in the multi-compartment Darcy model (the most upstream one) exchanges mass with the coronary outflows Γ^j. Thus, the volumetric source g_1 in (2b) should be provided by the outgoing coronary flow rate:

$$g_1(\boldsymbol{x}) = \sum_{j=1}^{J} \frac{\chi_{\Omega_M^j}(\boldsymbol{x})}{|\Omega_M^j|} \int_{\Gamma^j} \boldsymbol{u}_C \cdot \boldsymbol{n} d\gamma,$$

where the notation χ_A stands for the characteristic function of the domain A;

b) balance of interface forces: due to the heterogeneity of the two models and to the distributed nature of the Darcy model, we expect to have a pressure jump at the interface Γ^j which induces the following epicardial coronary flow rate [74]:

$$\int_{\Gamma^j} \boldsymbol{u}_C \cdot \boldsymbol{n} d\gamma = \alpha^j \left(\frac{1}{|\Gamma^j|} \int_{\Gamma^j} p_C(\boldsymbol{x}) d\boldsymbol{x} - \frac{1}{|\Omega_M^j|} \int_{\Omega_M^j} p_{M,1}(\boldsymbol{x}) d\boldsymbol{x} \right), \qquad j = 1, \dots, J,$$

where $\boldsymbol{n}$ is the unit outer normal vector and α^j the conductances (supposed to be dependent on the perfusion region). Notice that again only the first compartment is involved in the coupling condition and that we consider the average of pressure on the whole compartment Ω^j due to the homogenized nature of the Darcy equation.
The previous condition is *defective* since involves average quantities [73,26,53]. We therefore reformulate it into the following mixed pointwise/defective Robin condition, which guarantees enough boundary information for the normal component:

$$-p_C + \mu\left(\nabla \boldsymbol{u}_C + (\nabla \boldsymbol{u}_C)^T\right)\boldsymbol{n}\cdot\boldsymbol{n} + \frac{1}{\alpha^j}\int_{\Gamma^j} \boldsymbol{u}_C\cdot\boldsymbol{n}d\gamma = -\frac{1}{|\Omega_M^j|}\int_{\Omega_M^j} p_{M,1}(\boldsymbol{x})d\boldsymbol{x} \quad \text{on} \quad \Gamma^j,$$

where we have assumed a constant coronary normal traction over the section Γ^j.
Being a second order partial differential equation, the epicardial problem needs also a condition for the tangential components. Here, we assume that tangential tractions are null, i.e.:

$$\mu(\nabla \boldsymbol{u}_C + (\nabla \boldsymbol{u}_C)^T)\boldsymbol{n}\cdot\boldsymbol{\tau}_i = 0, \quad i = 1,2 \quad \text{on} \quad \Gamma^j,$$

where $\boldsymbol{\tau}_i$ are the two tangential unit vectors.

In what follows we summarize the whole coupled problem with its coupling conditions. In order to better highlight its properties in the case we are interested in, we write it directly for the case of three compartments ($N = 3$ in the multi-compartment Darcy model).

$$\rho\left(\frac{\partial \boldsymbol{u}_C}{\partial t} + (\boldsymbol{u}_C\cdot\nabla)\boldsymbol{u}_C\right) - \mu\nabla\cdot\left(\nabla \boldsymbol{u}_C + (\nabla \boldsymbol{u}_C)^T\right) + \nabla p_C = \boldsymbol{0} \qquad \text{in } \Omega_C, \tag{3a}$$

$$\nabla\cdot\boldsymbol{u}_C = 0 \qquad \text{in } \Omega_C, \tag{3b}$$

$$p_C - \mu\left(\nabla \boldsymbol{u}_C + (\nabla \boldsymbol{u}_C)^T\right)\boldsymbol{n}\cdot\boldsymbol{n} - \frac{1}{\alpha^j}\int_{\Gamma^j} \boldsymbol{u}_C\cdot\boldsymbol{n}d\gamma = \frac{1}{|\Omega_M^j|}\int_{\Omega_M^j} p_{M,1}d\boldsymbol{x} \qquad \text{on } \Gamma^j, \tag{3c}$$

$$\mu(\nabla \boldsymbol{u}_C + (\nabla \boldsymbol{u}_C)^T)\boldsymbol{n}\cdot\boldsymbol{\tau}_i = 0 \qquad i = 1,2 \qquad \text{on } \Gamma^j,$$

$$\boldsymbol{u}_{M,1} + \boldsymbol{K}_1\nabla p_{M,1} = \boldsymbol{0} \qquad \text{in } \Omega_M,$$

$$\nabla\cdot\boldsymbol{u}_{M,1} = \sum_{j=1}^{J}\frac{\chi_{\Omega_M^j}}{|\Omega_M^j|}\int_{\Gamma^j}\boldsymbol{u}_C\cdot\boldsymbol{n}d\gamma - \beta_{1,2}(p_{M,1} - p_{M,2}) \qquad \text{in } \Omega_M, \tag{3d}$$

$$\boldsymbol{u}_{M,2} + \boldsymbol{K}_2\nabla p_{M,2} = \boldsymbol{0} \qquad \text{in } \Omega_M,$$

$$\nabla\cdot\boldsymbol{u}_{M,2} = -\beta_{2,1}(p_{M,2} - p_{M,1}) - \beta_{2,3}(p_{M,2} - p_{M,3}) \qquad \text{in } \Omega_M,$$

$$\boldsymbol{u}_{M,3} + \boldsymbol{K}_3\nabla p_{M,3} = \boldsymbol{0} \qquad \text{in } \Omega_M,$$

$$\nabla\cdot\boldsymbol{u}_{M,3} = -\gamma(p_{M,3} - p_{veins}) - \beta_{3,2}(p_{M,3} - p_{M,2}) \qquad \text{in } \Omega_M,$$

where in the last equation we have accounted for the coronary venous return through p_{veins} which denotes the venous pressure and γ is a suitable coefficient. Parameters $\boldsymbol{K}_i$, $i = 1,2,3$, α^j, $j = 1,\dots,J$, and $\beta_{i,k}$, $i,k = 1,2,3$, need to be properly estimated. This will be the topic of the next section.

2.4. Generation of the intramural vascular network and parameter estimation

In order to provide the estimation of parameters $\boldsymbol{K}_i$, $i = 1,2,3$, α^j, $j = 1,\dots,J$, and $\beta_{i,k}$, $i,k = 1,2,3$, appearing in the coupled problem (3), we first need to generate a personalized intramural vascular network. Although this is not patient-specific, it is however built on patient data, such as the myocardial and the epicardial coronaries geometries. Indeed, while the epicardial coronaries can be reconstructed from in-vivo medical images, intramural vessels are too small to be visible in standard in-vivo clinical data. Thus, the intramural vascular network must be artificially generated starting from the available patient-specific geometries. With this aim, in Sect. 2.4.1 we introduce a new algorithm to obtain a partition of the myocardium in non-overlapping perfusion regions (see Section 2.3), whereas in Section 2.4.2 we describe the steps for the generation of the network. Finally, in Section 2.4.3 we detail the procedure for the estimation of the parameters.

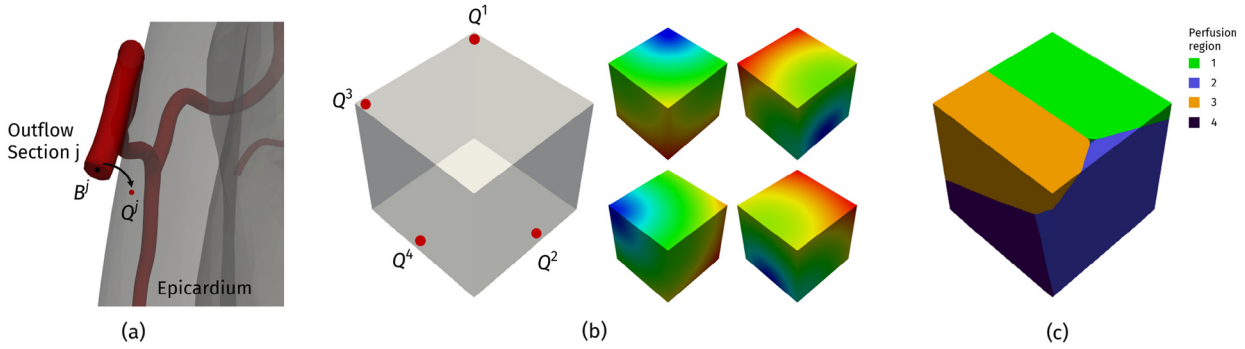


Fig. 3. The three main steps of the partitioning of the domain: (a) computing the closest epicardial point to the barycenter (projected outflows Q^j); (b) domain with 4 projected outflows and solution of the corresponding 4 eikonal problems; (c) corresponding perfusion regions.

2.4.1. Partitioning of the myocardium into perfusion regions

In this section, we describe the procedure used to partition the myocardial domain into non-overlapping perfusion regions. As highlighted before, each perfusing vessel feeds only one of such regions.

We state that a generic point P in the myocardium belongs to the perfusion region Ω_M^j, $j = 1, \dots, J$, if, among all the epicardial outflows, the section Γ^j is the closest one to P. Given P, to find j such that $P \in \Omega_M^j$, we propose the following steps, see Fig. 3:

1. for any outflow section Γ^j, $j = 1, \dots, J$, we look for the point Q^j such that

$$Q^j = \underset{P \in \partial\Omega_M}{\operatorname{argmin}} \|\boldsymbol{x}_P - \boldsymbol{x}_{B^j}\|,$$

   where $\boldsymbol{x}_P$ are the coordinates of P and B^j is the barycenter of Γ^j (see Fig. 3(a)). In other words, we look for the closest point of the epicardial surface $\partial\Omega_M$, named Q^j to Γ^j; for this reason we refer to Q^j as projected outflows;
2. for each $j = 1, \dots, J$, we solve the following eikonal problem:

$$|\nabla d^j| = 1 \qquad \text{in } \Omega_M, \tag{4a}$$

$$d^j = 0 \qquad \text{on } Q^j. \tag{4b}$$

   This allows us to compute for each point $\boldsymbol{x}$ of the myocardium the signed distance $d^j(\boldsymbol{x})$ from Γ^j (i.e. from its barycenter, see Fig. 3(b)). The application of the eikonal equation to compute a signed distance in meshes was used and analyzed in literature [23,16]. Fast Marching Method [40] and Fast Sweeping Method [31] are two of the most famous methods based on such approach;
3. finally, according to the definition of perfusion region provided above, we define Ω_M^j as follows (see Fig. 3c):

$$\Omega_M^j = \left\{ P \in \Omega_M : d^j(\boldsymbol{x}_P) = \min_{k=0,\dots,J} d^k(\boldsymbol{x}_P) \right\}.$$

2.4.2. Generation of the intramural vasculature network

To overcome the lack of anatomical data on the intramural vasculature, we propose here an algorithm to generate a personalized (although not patient-specific) intramural vascular network. This is inspired by the *bifurcating volume-filling network generation* algorithm proposed in [76,69], extended here to the case of non-convex geometries using an approach similar to the one proposed in [63], based on iso-potential surfaces constraint. Moreover, we have to specify the radius distribution along the network. With this aim, we suppose that at each bifurcation the radii of the daughter vessels follow the Murray's law:

$$r_\gamma^3 = r_\alpha^3 + r_\beta^3,$$

where r_γ is the radius of the parent vessel, whereas r_α and r_β are the radii of the daughter vessels.

The preliminary step of the procedure consists in subdividing the myocardial domain into right and left ventricles. Accordingly, referring to Fig. 4, we compute the solution of the following Laplace equation for the potential function Ψ between the epicardium ($\partial\Omega_{epi}$) and the endocardium of the right and the left ventricles ($\partial\Omega_{rv}$ and $\partial\Omega_{lv}$, respectively) [7]:

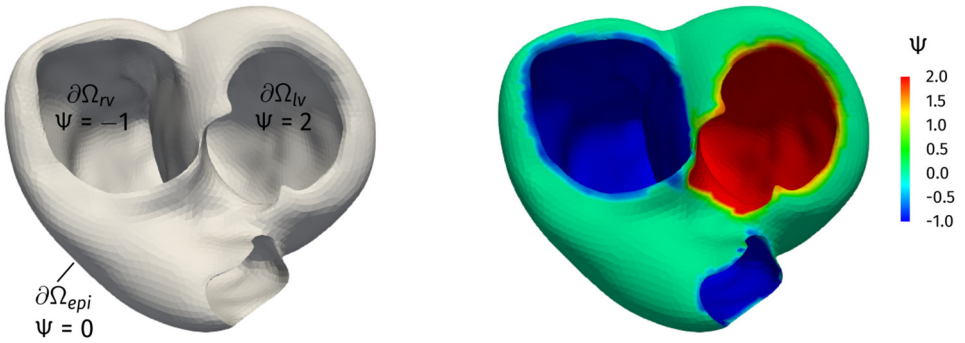


Fig. 4. The biventricle domain (on the left) and the Laplace solution (on the right). (For interpretation of the colors in the figure(s), the reader is referred to the web version of this article.)

$$\Delta\Psi = 0 \qquad \text{in } \Omega_M, \tag{5a}$$

$$\Psi = 0 \qquad \text{on } \partial\Omega_{epi}, \tag{5b}$$

$$\Psi = -1 \qquad \text{on } \partial\Omega_{rv}, \tag{5c}$$

$$\Psi = 2 \qquad \text{on } \partial\Omega_{lv}. \tag{5d}$$

The boundary conditions are chosen to distinguish the two ventricles walls. Indeed, we create a positive (resp. negative) gradient potential inside the left (resp. right) ventricle wall (Fig. 4) and the values ($\Psi = 2$ and $\Psi = -1$, respectively) allow to assign two thirds of the septum to the left ventricle and one third to the right ventricle, according to experimental evidence [21,28,2,59,11]. In particular, if there exist $\boldsymbol{x}_1$ and $\boldsymbol{x}_2 \in \Omega_M^j$ s.t. $\Psi(\boldsymbol{x}_1)\,\Psi(\boldsymbol{x}_2) < 0$, then the perfusion region Ω_M^j is split into the two subdomains $\Omega_M^{j,lv}$ and $\Omega_M^{j,rv}$ that will be treated as single perfusion regions from now on (with an abuse of notation we will still use Ω_M^j to refer to such regions).

The following step consists in another pre-process of the myocardium to allow the vascular network generation in the domain Ω_M. Indeed, the *bifurcating volume-filling network generation* algorithm [76,69] in its standard definition is not enough to generate a network inside a non-convex geometry like the myocardial one. For this reason, similarly to [63], we want to define isopotential volumes inside the myocardium to address the vascular network generation in a first phase in which the generated vessels cover part of the topology of the epicardial surface. In a second phase the following vessels penetrate and "fill" the walls of the myocardium.

To this aim, for each perfusion region Ω_M^j, we build N_{iso} isopotential surfaces that will be used to find a set of layers L_ℓ, $\ell = 0, \ldots, N_{iso} - 1$, inside Ω_M^j, defined as the volumes included between two consecutive isopotential surfaces. Then we use these layers to distinguish two different zones of the myocardial wall, one for each phase of the vessel generation: the first one, defined as the set of layers L_ℓ with $\ell = 0, \ldots, N_{iso-epi} << N_{iso}$, where the vessels grow according to the topology of the epicardial surface and the second one, corresponding to the internal layers $N_{iso-epi} < \ell < N_{iso}$, where the vessels penetrate the myocardial wall.

The last step of the procedure consists in the network generation itself, see Fig. 5. To generate the vessels in the first zone, for each perfusion region Ω_M^j, we consider a double loop with indices ℓ for the layers and m for the volumes generated within a layer. We start from layer $\ell = 0$, we define the nodes $\boldsymbol{x}_{B,1}^{-1} = \boldsymbol{x}_{*,1}^{-1} = B^j$ (B^j being the barycenter of the outflow section Γ^j, cf Fig. 3(a)) and $\boldsymbol{x}_{B,1}^{-2} = \boldsymbol{O}$, and we set $\Upsilon_1^0 = \Omega_M^j$. Thus, remembering that $\lceil y/x \rceil$ indicates the superior integer part (ceiling) of y/x, we have Algorithm 1.

Algorithm 1 Generation of the intramural network.

for $\ell = 0, \ldots, N_{iso-epi} - 1$ **do**
  for $m = 1, \ldots, 2^\ell$ **do**
    Compute the barycenter $\boldsymbol{x}_{B,m}^\ell$ of the volume Υ_m^ℓ;
    Find the point $\boldsymbol{y}_{B,m}^\ell = \underset{P \in L_\ell \cap \Upsilon_m^\ell}{\operatorname{argmin}} \|\boldsymbol{x}_P - \boldsymbol{x}_{B,m}^\ell\|$;
    Compute the midpoint $\boldsymbol{z}_m^\ell = \dfrac{\boldsymbol{y}_{B,m}^\ell - \boldsymbol{x}_{*,\lceil m/2 \rceil}^{\ell-1}}{2}$;
    Find the point $\boldsymbol{x}_{*,m}^\ell = \underset{P \in L_\ell \cap \Upsilon_m^\ell}{\operatorname{argmin}} \|\boldsymbol{x}_P - \boldsymbol{z}_m^\ell\|$;
    Generate a new vessel considering the line going from $\boldsymbol{x}_{*,\lceil m/2 \rceil}^{\ell-1}$ to $\boldsymbol{x}_{*,m}^\ell$;
    Split the domain Υ_m^ℓ into two subdomains $\Upsilon_{2m-1}^{\ell+1}$ and $\Upsilon_{2m}^{\ell+1}$ using the plane passing through the points $\boldsymbol{x}_{B,m}^\ell$, $\boldsymbol{x}_{B,\lceil m/2 \rceil}^{\ell-1}$ and $\boldsymbol{x}_{B,\lceil m/4 \rceil}^{\ell-2}$;
  end for
end for

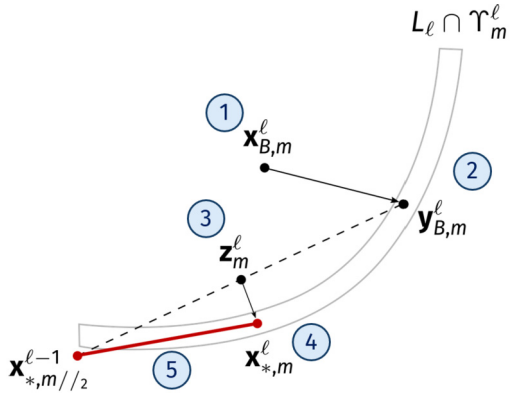


Fig. 5. Procedure to generate the vessels in the first zone of the myocardial wall.

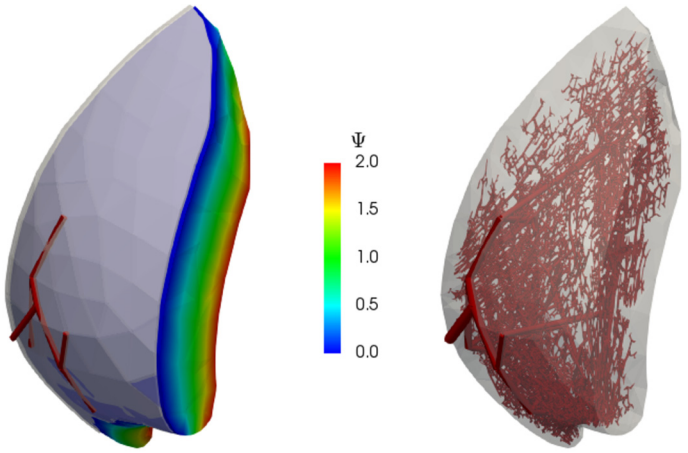


Fig. 6. Example of a generated network inside a partition region: on the left the first $2^{N_{iso-epi}} - 1$ vessels in the case $N_{iso-epi} = 3$, the first zone (in grey) and the Laplace solution; on the right the complete network.

This procedure allows us to create for each level ℓ exactly 2^ℓ volumes Υ^ℓ_m (Fig. 5). Each volume contains the terminal point of a vessel of the network. Notice also that $\Upsilon^{\ell-1}_{m//_2}$ is the parent volume of Υ^ℓ_m, whereas $\Upsilon^{\ell-2}_{m//_4}$ its grandparent. With respect to the algorithm proposed in [76,69], we added here the solution of the Laplacian (5) and the definition of the layers L_ℓ. This allows us to create vessels that better follow the morphology of the epicardium. This is possible thanks to the definition of points $\boldsymbol{x}^\ell_{*,m}$ used to generate the vessels instead of the barycenters $\boldsymbol{x}^\ell_{B,m}$ as done in [76,69]. The use of barycenters would not be optimal in our case since the non-convexity of the domain would lead to barycenters outsides the volume.

Finally, regarding the second zone (the inner layers L_ℓ, $\ell > N_{iso-epi}$), we consider the generation of the vessels using the original algorithm in [76,69]. This is motivated by the fact that for the inner layers the domains are regular and convex. The generation stops if the radius of a daughter vessel is less than R_{min}. In this work, we have set $R_{min} = 30$ µm. This means that, in order to reduce the complexity, we do not generate vessels in the microvasculature. Thus, since we want to correlate the third compartment to the microvasculature, but we do not generate the corresponding vessels of the network, we choose to associate the intramural vascular network only to the first and second compartment (see Section 2.2), and not correlate any vessel to the third one.

Other approaches have been proposed in the literature for the generation of a coronary network and in particular to determine the bifurcation angle, introducing anatomical and physiological information. For example, in [38] the authors generated a coronary network by using the anatomical data from [39] and with a bifurcation angle taken from [81,82]. Instead, in [65] the authors, starting again from the data reported in [39], used a bifurcation angle based on the minimization of the shear rate [80], whereas in [36] physiological constraints are introduced by means of the Constraint Constructive Optimization (CCO) method [62], which relies on hemodynamics principles. Here, for the sake of simplicity we preferred to use a pure geometric criterion to generate the network. We stress that the aim of our algorithm is to generate a personalized-surrogate network to be used only to estimate the parameters and not to directly compute blood dynamics quantities.

An example of the results of the proposed procedure is shown in Fig. 6.

2.4.3. Estimation of the multi-compartment model parameters

Once we have generated a vascular network for the intramural vessels, we can consider the estimation of parameters $\boldsymbol{K}_i$, $i = 1, 2, 3$, α^j, $j = 1, \ldots, J$, and $\beta_{i,k}$, $i, k = 1, 2, 3$, in (3).

The first step consists in the separation of the intramural vascular network into two groups of vessels using a specific metric. This is motivated by the fact that we can relate the largest vessels to the first compartment, whereas the smallest ones to the second compartment (remember that we do not have vessels in the third compartment). To perform such operation, a hierarchic parameter $\zeta \in [0, 1]$ is defined for each node $\boldsymbol{y}_i$ of the network. Following the approach used in [34,35], $\zeta(\boldsymbol{y}_i)$ is defined as the ratio between the sum of the lengths of the vessels which are located distally to $\boldsymbol{y}_i$ and the sum of the lengths of all the vessels of the network. In this way ζ will be 1 for the most proximal nodes and 0 for the most distal terminal nodes. Then, given for each perfusion region Ω_M^j a value $Z^j \in (0, 1)$, we sort a vessel of the network to belong to the first (resp. second) group if the average of the values of ζ in the nodes of the vascular network at hand is in the range $[0, Z^j)$ (resp. $[Z^j, 1]$). The values Z^j are chosen in order to have about the same number of vessels in the two groups.

Let $\boldsymbol{K}_i^j$ be the permeability tensor of the i-th compartment in the perfusion region Ω_M^j. Following [34], we assume that this tensor is isotropic:

$$\boldsymbol{K}_i^j = \phi_i^j \boldsymbol{I},$$

where $\boldsymbol{I}$ is the identity tensor with unit of $\mathrm{cm}^2\,\mathrm{Pa}^{-1}\,\mathrm{s}^{-1}$ and ϕ_i^j is the constant porosity. The latter is defined as follows:

$$\phi_i^j = \frac{\sum_{n=1}^{M_i^j} V_{i,n}^j}{V_{\Omega_M^j}},$$

where $V_{\Omega_M^j}$ is the volume of Ω_M^j, M_i^j the number of the vessels in Ω_M^j, and $V_{i,n}^j$ the volume of the n-th vessel in the i-th compartment of Ω_M^j. Finally, the global piecewise constant permeability tensor $\boldsymbol{K}_i$ is defined as

$$\boldsymbol{K}_i(\boldsymbol{x}) = \sum_{j=1}^{J} \boldsymbol{K}_i^j \chi_{\Omega_M^j}(\boldsymbol{x}).$$

The choice of an isotropic tensor is motivated by the observation made in [34] that the error between the Poiseuille and the multi-compartment pressures is smaller with respect to that obtained by using an anisotropic tensor.

To compute parameters $\beta_{i,k}$ and α^j, the geometric description of the network is not enough. We need also information about the pressure and flow distributions in the vascular network. In order to find an approximation of them, we consider the solution of a Poiseuille flow problem along vascular network, given by the union between the epicardial coronaries and the intramural network. To reduce the computational effort, we consider the epicardial coronaries as 1D models (notice that this is done only here for the parameter estimation, whereas elsewhere in the model the coronaries are 3D). As for the boundary conditions, we prescribe an inlet pressure of 109 mmHg [14] and outlet pressures depending on the radius of the terminal vessels [14]. A constant multiplicative correction factor η is in case applied to all the vessels radii in order to obtain a physiological flow rate starting from this pressure gradient. In our case, we adopt $\eta = 2.3$.

Referring to this Poiseuille solution, let $Q_{i,k}^j = Q_{k,i}^j$, $i, k = 1, 2, 3$, be the total flow rate exchanged in the perfusion region Ω_M^j at the interface between compartment i and compartment k. Since we do not have vessels in the third compartment, we set $Q_{2,3}^j$ to be equal to the total flow rate at the outlet of the second compartment of Ω_M^j. Moreover, let $p_{i,n}^j$, $i = 1, 2$, be the pressure in the n-th vessel of compartment i in the perfusion region Ω_M^j and $\overline{p}_3^j = 39$ mmHg a reference value for the microvasculature pressure for all j, computed as the average value between the pressure of the most downstream vessels ($\simeq 56$ mmHg [14]) and the value of $p_{veins} = 22.5$ mmHg [35]. Thus, introducing the local coupling coefficient $\beta_{i,k}^j$ inside the perfusion region Ω_M^j (symmetric over the indices i and k), we have [34]:

$$\beta_{1,2}^j = \begin{cases} 0 & \text{if } \overline{p}_1^j - \overline{p}_2^j = 0, \\ \dfrac{\overline{Q}_{1,2}^j}{|\overline{p}_1^j - \overline{p}_2^j|} & \text{otherwise,} \end{cases} \qquad \beta_{2,3}^j = \begin{cases} 0 & \text{if } \overline{p}_2^j - \overline{p}_3^j = 0, \\ \dfrac{\overline{Q}_{2,3}^j}{|\overline{p}_2^j - \overline{p}_3^j|} & \text{otherwise,} \end{cases} \qquad \beta_{i,k}^j = 0 \quad \text{elsewhere,}$$

where

$$\overline{Q}_{i,k}^j = \frac{Q_{i,k}^j}{V_{\Omega_M^j}}$$

and

$$\overline{p}_i^j = \frac{\sum_{n=1}^{M_i^j} p_{i,n}^j V_{i,n}^j}{\sum_{n=1}^{M_i^j} V_{i,n}^j} \; i = 1, 2. \tag{6}$$

As done before for the permeability $\boldsymbol{K}_i$, the global piecewise constant inter-compartment coupling coefficient $\beta_{i,k}$ is defined as:

$$\beta_{i,k}(\boldsymbol{x}) = \sum_{j=1}^{J} \beta_{i,k}^j \chi_{\Omega_M^j}(\boldsymbol{x}).$$

In a similar way the conductance coefficient α^j is computed as:

$$\alpha^j = \frac{Q_{inlet}^j}{|p_{inlet}^j - \overline{p}_1^j|}, \quad j = 1, \ldots, J,$$

where Q_{inlet}^j is the flow rate entering in the first compartment of Ω_M^j and p_{inlet}^j is the pressure in the first node of the first compartment of Ω_M^j.

We observe that the intramural topology obtained using our strategy has no direct impact on the mathematical model formulation since the network is used only for parameters estimation. We stress that the characteristics of the vascular network that may have a major impact on the values of the multi-compartment model parameters are the vessel length, since this could determine the belonging of the vessel to one Darcy compartment or to another one, and the value of the vessel radii, since this would heavily influence the downstream resistances.

Remark 1. We notice that similar strategies to those reported in the previous sections have been used in computational mechanics for lungs. For example, a similar approach to ensure mass conservation has been considered in [79] for the coupling between the upper airways and the parenchyma, whereas in [78] a 3D-1D coupling between the upper and lower airways with an algorithm to generate a surrogate network for the latter and the use of one-to-one correspondence between each terminal bronchiole and a specific lung region, similar to our perfusion regions, have been proposed. We also mention [8] where a subdivision of the porous region in distinct subdomains with interface mass conservation conditions has been considered.

3. Numerical approximation

In this section we describe the numerical methods used to solve the problems addressed above. In particular, for the spatial discretization of problems (4), (3) and (5) we use the Finite Element method for spatial discretization in combination with the Finite Difference method for time discretization. To this purpose we have created two volumetric tetrahedral meshes, one for Ω_C and one for Ω_M. Moreover, for an effective numerical solution of the coupled problem (3), we propose an iterative splitting strategy for the solution and an efficient numerical strategy to solve the corresponding linear systems.

3.1. Time and finite element discretizations

We adopt P_1 Finite Elements for both the eikonal problem (4) and the Laplace equation (5). We recall that the standard FE discretization of the eikonal equation is unstable; in order to stabilize it, we add an artificial diffusion term $\epsilon \Delta d^j$, with $\epsilon = h_{max}/2$ and where h_{max} is the maximum cell diameter of the mesh of Ω_M.

Regarding problem (3), for the time discretization we subdivide the time interval $[0, T]$ into N_t subintervals of dimension $\Delta t = \frac{T}{N_t}$ and the time steps are defined as $t^n = n\Delta t$ for $n = 0, \ldots, N_t$. Accordingly, given a function of time $z(t)$, we indicate with z^n the approximation of $z(t^n)$. Then, for the fluid problem (3a)-(3b), we use a backward differentiation formula of order 1 and we treat the convective term in a semi-implicit way [56]. This introduces a CFL-like restriction on the time discretization parameter, $\Delta t \lesssim h_{min}$, where h_{min} is the minimum cell diameter of the mesh of Ω_C. As for the spatial discretization, we consider P_1/P_1 Finite Elements with a SUPG-PSPG stabilization [70,72,25,27] for (3a)-(3b), whereas we adopt $\boldsymbol{RT}_0/P_0$ Finite Elements for the multi-compartment Darcy problem.

3.2. Iterative splitting strategy

For the numerical solution of the coupled problem (3) a monolithic (one shot) approach would be very demanding in terms of computational costs. For this reason, we propose an iterative strategy based on the splitting of the problem into two sub-problems which are solved sequentially. This idea is based on the heterogeneous Domain Decomposition approach for multi-physics problems, see [56]. Examples of splitting algorithms in such context are given, e.g., by [18,5] for the fluid-structure interaction problem, [20] for the Stokes-Darcy coupling, [10] for the 3D-1D geometric multiscale coupling, [57] for the liver perfusion coupled problem. In particular, the idea is to equip the fluid problem with a Neumann boundary

condition coming from the Robin interface condition (3c), and to provide to the first (most upstream) Darcy problem a mass term coming from (3d). The iterations read as follows:
Let the current temporal index $n+1$ be omitted for the notation; then, we propose the iterative procedure described in Algorithm 2, where s is the current iteration, ε_{tol} is a given tolerance, $diff_x = \frac{\|x^{(s)} - x^{(s-1)}\|}{\|x^{(s)}\|}$ and the norm has to be intended in $[H^1]^3$ for the velocities and L^2 for the pressures.

Algorithm 2 Iterative splitting strategy.

1: **for** $n = 1 \dots N_t$ **do**
2: **while** $max(diff_{\boldsymbol{u}_C}; diff_{p_C}; diff_{\boldsymbol{u}_{M,1}}; diff_{p_{M,1}}) > \varepsilon_{tol}$ **do**
3: Solve the fluid problem at iteration s:

$$\rho\left(\frac{\boldsymbol{u}_C^{(s)} - \boldsymbol{u}_C^n}{\Delta t} + (\boldsymbol{u}_C^n \cdot \nabla)\boldsymbol{u}_C^{(s)}\right) - \mu\nabla\cdot\left(\nabla\boldsymbol{u}_C^{(s)} + \left(\nabla\boldsymbol{u}_C^{(s)}\right)^T\right) + \nabla p_C^{(s)} = \boldsymbol{0} \qquad \text{in } \Omega_C, \tag{7a}$$

$$\nabla\cdot\boldsymbol{u}_C^{(s)} = 0 \qquad \text{in } \Omega_C, \tag{7b}$$

$$-p_C^{(s)} + \mu\left(\nabla\boldsymbol{u}_C^{(s)} + (\nabla\boldsymbol{u}_C^{(s)})^T\right)\boldsymbol{n}\cdot\boldsymbol{n} = -\frac{1}{|\Omega_M^j|}\int_{\Omega_M^j} p_{M,1}^{(s-1)} d\boldsymbol{x} - \frac{1}{\alpha^j}\int_{\Gamma^j} \boldsymbol{u}_C^{(s-1)}\cdot\boldsymbol{n} d\gamma \qquad \text{on } \Gamma^j, \tag{7c}$$

$$\mu(\nabla\boldsymbol{u}_C^{(s)} + (\nabla\boldsymbol{u}_C^{(s)})^T)\boldsymbol{n}\cdot\boldsymbol{\tau}_i = 0 \qquad i = 1,2 \qquad \text{on } \Gamma^j; \tag{7d}$$

4: Solve the multi-compartment Darcy problem at iteration s:

$$\boldsymbol{u}_{M,1}^{(s)} + \boldsymbol{K}_1\nabla p_{M,1}^{(s)} = \boldsymbol{0} \qquad \text{in } \Omega_M, \tag{8a}$$

$$\nabla\cdot\boldsymbol{u}_{M,1}^{(s)} = \sum_{j=1}^{J}\frac{\chi_{\Omega_M^j}}{|\Omega_M^j|}\int_{\Gamma^j}\boldsymbol{u}_C^{(s)}\cdot\boldsymbol{n} d\gamma - \beta_{1,2}(p_{M,1}^{(s)} - p_{M,2}^{(s)}) \qquad \text{in } \Omega_M, \tag{8b}$$

$$\boldsymbol{u}_{M,2}^{(s)} + \boldsymbol{K}_2\nabla p_{M,2}^{(s)} = \boldsymbol{0} \qquad \text{in } \Omega_M, \tag{8c}$$

$$\nabla\cdot\boldsymbol{u}_{M,2}^{(s)} = -\sum_{k=1}^{3}\beta_{2,k}(p_{M,2}^{(s)} - p_{M,k}^{(s)}) \qquad \text{in } \Omega_M, \tag{8d}$$

$$\boldsymbol{u}_{M,3}^{(s)} + \boldsymbol{K}_3\nabla p_{M,3}^{(s)} = \boldsymbol{0} \qquad \text{in } \Omega_M, \tag{8e}$$

$$\nabla\cdot\boldsymbol{u}_{M,3}^{(s)} = -\gamma(p_{M,3}^{(s)} - p_{veins}) - \beta_{3,2}(p_{M,3}^{(s)} - p_{M,2}^{(s)}) \qquad \text{in } \Omega_M; \tag{8f}$$

5: $s \to s+1$;
6: **end while**
7: **end for**

We considered two versions of this algorithm: the first one is fully explicit, in which we perform only one iteration per time step, whereas the second one is implicit, which means that we continue to subiterate until convergence. In the first case, we expect to have another bound on Δt to ensure stability of the scheme. However the numerical experiments showed that this constraint is milder than the CFL one coming from the semi-implicit treatment for the discretization of the Navier-Stokes problem.

In what follows, we provide a convergence analysis of a simplified linearized version of Algorithm 2. To do this, we consider, for the sake of simplicity, the Stokes equations for the 3D fluid problem at step 3, constant scalar permeabilities K_i and just one outflow Γ. Moreover, since the coupled problem is linear, we are interested at each time step in the convergence towards the null solution, thus we set to zero the forcing terms and the quantities at previous time step. We refer to this algorithm as Algorithm 2bis. Thus, we have the following result.

Proposition 1. *Consider Algorithm 2bis defined above. Then, given $\varepsilon > 0$ small enough, under the following hypotheses on the parameters*

$$K_1 > K_2, \tag{9a}$$

$$\beta_{2,3}(K_2 - \varepsilon K_3) \geq \beta_{1,2}(K_1 - K_2), \tag{9b}$$

$$\gamma \geq \frac{1-2\varepsilon}{2\varepsilon} - \frac{K_2\beta_{2,3}}{2K_3}, \tag{9c}$$

$$\mu > \frac{2K_1C_T^2|\Gamma|^{1/2}}{|\Omega_M|\beta_{1,2}(K_1 - K_2)}, \tag{9d}$$

$$\Delta t < \frac{\rho}{\mu}, \tag{9e}$$

there exists a constant C with $0 < C < 1$ such that the algorithm is a contraction with respect to the interface variable $p_{M,1}$, i.e.

$$\|p_{M,1}^{(s)}\|_{L^2(\Omega_M)} \leq C\|p_{M,1}^{(s-1)}\|_{L^2(\Omega_M)}.$$

Proof. From now on, if not specified, the current iteration s will be understood.

We start from the weak formulation of the 3D fluid problem at step 3. We obtain, for $\boldsymbol{u}_C$, $\boldsymbol{v}_C \in [H^1(\Omega_C)]^3$ and $p_C \in L^2(\Omega_C)$:

$$\frac{\rho}{\Delta t}\int_{\Omega_C} \boldsymbol{u}_C \cdot \boldsymbol{v}_C + \mu \int_{\Omega_C} \nabla \boldsymbol{u}_C : \nabla \boldsymbol{v}_C - \int_{\Omega_C} p_C \nabla \cdot \boldsymbol{v}_C + \frac{1}{\alpha}\int_{\Gamma} \boldsymbol{u}_C \cdot \boldsymbol{n} \int_{\Gamma} \boldsymbol{v}_C \cdot \boldsymbol{n} = -\frac{1}{|\Omega_M|}\int_{\Omega_M} p_{M,1}^{(s-1)} \int_{\Gamma} \boldsymbol{v}_C \cdot \boldsymbol{n},$$

where, for the sake of simplicity, we have taken the term $\frac{1}{\alpha^j}\int_{\Gamma^j} \boldsymbol{u}_C^{(s)} \cdot \boldsymbol{n} d\gamma$ in the Robin condition at the current iteration. Taking $\boldsymbol{v}_C = \boldsymbol{u}_C$, we obtain

$$\xi \|\boldsymbol{u}_C\|^2_{H^1(\Omega_C)} \leq \frac{1}{|\Omega_M|}\int_{\Omega_M} p_{M,1}^{(s-1)} C_T \|\boldsymbol{u}_C\|_{H^1(\Omega_C)},$$

where C_T is the constant of the trace inequality and $\xi = \min\{\rho/\Delta t; \mu\}$. Thus, from the Cauchy-Schwarz inequality, we have

$$\|\boldsymbol{u}_C^{(s)}\|_{H^1(\Omega_C)} \leq \frac{C_T}{\xi |\Omega_M|^{1/2}} \|p_{M,1}^{(s-1)}\|_{L^2(\Omega_M)}. \tag{10}$$

Consider now the multi-compartment Darcy problem at step 4. Its weak formulation, for $\boldsymbol{u}_{M,i}$, $\boldsymbol{v}_M \in [H^1_{div,0}(\Omega_M)]^3$ and $p_{M,i}, q_M \in L^2(\Omega_M)$, reads:

$$\begin{aligned}
&\int_{\Omega_M} \boldsymbol{u}_{M,1} \cdot \boldsymbol{v}_M - K_1 \int_{\Omega_M} p_{M,1} \nabla \cdot \boldsymbol{v}_C = 0,\\
&\int_{\Omega_M} \nabla \cdot \boldsymbol{u}_{M,1} q_M = \frac{1}{|\Omega_M|}\int_{\Gamma} \boldsymbol{u}_C \cdot \boldsymbol{n} \int_{\Omega_M} q_M - \beta_{1,2}\int_{\Omega_M} (p_{M,1} - p_{M,2}) q_M,\\
&\int_{\Omega_M} \boldsymbol{u}_{M,2} \cdot \boldsymbol{v}_M - K_2 \int_{\Omega_M} p_{M,2} \nabla \cdot \boldsymbol{v}_C = 0,\\
&\int_{\Omega_M} \nabla \cdot \boldsymbol{u}_{M,2} q_M = -\beta_{2,1}\int_{\Omega_M} (p_{M,2} - p_{M,1}) q_M - \beta_{2,3}\int_{\Omega_M} (p_{M,2} - p_{M,3}) q_M,\\
&\int_{\Omega_M} \boldsymbol{u}_{M,3} \cdot \boldsymbol{v}_M - K_3 \int_{\Omega_M} p_{M,3} \nabla \cdot \boldsymbol{v}_C = 0,\\
&\int_{\Omega_M} \nabla \cdot \boldsymbol{u}_{M,1} q_M = -\gamma \int_{\Omega_M} p_{M,3} q_M - \beta_{3,2}\int_{\Omega_M} (p_{M,3} - p_{M,2}) q_M.
\end{aligned}$$

By taking $\boldsymbol{v}_M = \boldsymbol{u}_{M,i}$, $i = 1, 2, 3$ in the first, third and fifth equation, respectively, and $q_M = p_{M,i}$, $i = 1, 2, 3$ in the second, fourth and sixth equation, respectively, and then summing up, we obtain

$$\begin{aligned}
&\sum_{i=1}^{3} \|\boldsymbol{u}_{M,i}\|^2_{L^2(\Omega_M)} + K_1 \int_{\Omega_M} \beta_{1,2}(p_{M,1} - p_{M,2}) p_{M,1} + K_2 \int_{\Omega_M} \beta_{1,2}(p_{M,2} - p_{M,1}) p_{M,2} + K_2 \int_{\Omega_M} \beta_{2,3}(p_{M,2} - p_{M,3}) p_{M,2}\\
&+ K_3 \int_{\Omega_M} \beta_{2,3}(p_{M,3} - p_{M,2}) p_{M,3} + \gamma \|p_{M,3}\|_{L^2(\Omega_M)} = K_1 \frac{1}{|\Omega_M|}\int_{\Gamma} \boldsymbol{u}_C \cdot \boldsymbol{n} \int_{\Omega_M} p_{M,1}.
\end{aligned}$$

From the Young inequality applied to the mixed pressure terms, we obtain

$$\begin{aligned}
&\left(\frac{K_1\beta_{1,2}}{2} - \frac{K_2\beta_{1,2}}{2}\right)\|p_{M,1}\|^2_{L^2(\Omega_M)} + \left(-\frac{K_1\beta_{1,2}}{2} + \frac{K_2\beta_{1,2}}{2} + \frac{K_2\beta_{2,3}}{2} - \varepsilon\frac{K_3\beta_{2,3}}{2}\right)\|p_{M,2}\|^2_{L^2(\Omega_M)}\\
&+ \left(-\frac{K_2\beta_{2,3}}{2} + \frac{K_3\beta_{2,3}}{2\varepsilon} + \gamma K_3\right)\|p_{M,3}\|^2_{L^2(\Omega_M)} \leq \frac{K_1 C_T |\Gamma|^{1/2}}{|\Omega_M|^{1/2}} \|\boldsymbol{u}_C\|_{H^1(\Omega_C)} \|p_{M,1}\|_{L^2(\Omega_M)},
\end{aligned}$$

where $\varepsilon > 0$ is used for the term $\int_{\Omega_M} K_3 \beta_{2,3} p_{M,2} p_{M,3}$. Owing to hypotheses (9), we have

$$\|p_{M,1}^{(s)}\|_{L^2(\Omega_M)} \leq \frac{2K_1 C_T |\Gamma|^{1/2}}{|\Omega_M|^{1/2} \beta_{1,2}(K_1 - K_2)} \|\boldsymbol{u}_C^{(s)}\|_{H^1(\Omega_C)}.$$

By inserting (10) in the previous inequality, we obtain

$$\|p_{M,1}^{(s)}\|_{L^2(\Omega_M)} \leq \frac{2K_1 C_T |\Gamma|^{1/2}}{|\Omega_M|^{1/2} \beta_{1,2}(K_1 - K_2)} \frac{C_T}{\xi |\Omega_M|^{1/2}} \|p_{M,1}^{(s-1)}\|_{L^2(\Omega_M)} = C \|p_{M,1}^{(s-1)}\|_{L^2(\Omega_M)}.$$

Thanks to hypotheses (9), we have $0 < C < 1$ and thus the thesis follows. □

Remark 2. In the numerical experiments often $K_2 < K_3$ (as for example in Test I reported in Section 4.1). Thus, we introduced ε in the previous proof in order to make positive the left hand side of the second hypothesis (9).

Hypothesis $K_1 > K_2$ follows, e.g., if, as in our case, the number of vessels in compartments 1 and 2 is the same. Since the dimension of the vessels in the first compartment is greater, this implies that the porosity there is larger. The hypothesis on the lower bound for γ guarantees that the resistance of the venous tract downstream the capillaries is small enough to allow the exit of blood from the latter. The hypothesis on Δt is very mild since the right hand side is of the order of seconds.

The existence of a fixed point for Algorithm 2bis ensures the well-posedness of the corresponding unsplit problem. Notice also that the analysis should be easily extended (owing to suitable technicalities) to the case of many outlets and non-constant permeabilities, whereas the extension to the Navier-Stokes case requires the treatment of the non-linear term which should guarantee estimate (10) provided that the data (and then $\boldsymbol{u}_C$) are small enough.

3.3. Numerical solvers

We detail here the numerical solvers used to solve the two subproblems (7) and (8) appearing at each iteration of the previous iterative algorithm.

The algebraic linear system associated to the fluid problem (7) is solved using the preconditioned GMRES. In particular, we consider the SIMPLE preconditioner in its approximated formulation (aSIMPLE) [19].

Regarding the multi-compartment Darcy problem (8), we start defining the corresponding algebraic system (omit for the sake of simplicity the iteration index s):

$$\begin{bmatrix} \mathbb{A}_1 & \mathbb{B}^T & \mathbb{O} & \mathbb{O} & \mathbb{O} & \mathbb{O} \\ \mathbb{B} & \mathbb{C}_{12} & \mathbb{O} & -\mathbb{C}_{12} & \mathbb{O} & \mathbb{O} \\ \mathbb{O} & \mathbb{O} & \mathbb{A}_2 & \mathbb{B}^T & \mathbb{O} & \mathbb{O} \\ \mathbb{O} & -\mathbb{C}_{21} & \mathbb{B} & \mathbb{C}_{21} + \mathbb{C}_{23} & \mathbb{O} & -\mathbb{C}_{23} \\ \mathbb{O} & \mathbb{O} & \mathbb{O} & \mathbb{O} & \mathbb{A}_3 & \mathbb{B}^T \\ \mathbb{O} & \mathbb{O} & \mathbb{O} & -\mathbb{C}_{32} & \mathbb{B} & \mathbb{C}_{32} + \mathbb{C}_\gamma \end{bmatrix} \begin{bmatrix} \mathbf{U}_{M,1} \\ \mathbf{P}_{M,1} \\ \mathbf{U}_{M,2} \\ \mathbf{P}_{M,2} \\ \mathbf{U}_{M,3} \\ \mathbf{P}_{M,3} \end{bmatrix} = \begin{bmatrix} \mathbf{O} \\ \mathbf{G}_1(\mathbf{U}_C) \\ \mathbf{O} \\ \mathbf{O} \\ \mathbf{O} \\ \mathbf{G}_3 \end{bmatrix}, \tag{11}$$

where, for each compartment $i = 1, 2, 3$, $\mathbf{U}_{M,i}$ and $\mathbf{P}_{M,i}$ are the velocity and the pressure vectors of unknowns, respectively, $\mathbf{G}_i$ is the vector accounting for the source term (notice in particular the dependence of $\mathbf{G}_1$ on the epicardial coronary velocity $\mathbf{U}_C$). Moreover, let $\boldsymbol{\psi}_j$ and φ_ℓ the basis functions related to the velocity and pressure, respectively. Thus we have $(\mathbb{A}_i)_{jp} = \int_{\Omega_M} (\boldsymbol{K}_i^{-1} \boldsymbol{\psi}_p) \cdot \boldsymbol{\psi}_j$, $\mathbb{B}_{\ell j} = -\int_{\Omega_M} \nabla \cdot \boldsymbol{\psi}_j \varphi_\ell$, $(\mathbb{C}_{ik})_{\ell m} = \int_{\Omega_M} \beta_{i,k} \varphi_m \varphi_\ell$, $(\mathbb{C}_\gamma)_{\ell m} = \int_{\Omega_M} \gamma \varphi_m \varphi_\ell$.

To solve the linear system (11), we consider a block diagonal preconditioner $\mathbb{P}$ defined as follows:

$$\mathbb{P} = \begin{bmatrix} \mathbb{A}_1 & \mathbb{B}^T & \mathbb{O} & \mathbb{O} & \mathbb{O} & \mathbb{O} \\ \mathbb{B} & \mathbb{C}_{12} & \mathbb{O} & \mathbb{O} & \mathbb{O} & \mathbb{O} \\ \mathbb{O} & \mathbb{O} & \mathbb{A}_2 & \mathbb{B}^T & \mathbb{O} & \mathbb{O} \\ \mathbb{O} & \mathbb{O} & \mathbb{B} & \mathbb{C}_{21} + \mathbb{C}_{23} & \mathbb{O} & \mathbb{O} \\ \mathbb{O} & \mathbb{O} & \mathbb{O} & \mathbb{O} & \mathbb{A}_3 & \mathbb{B}^T \\ \mathbb{O} & \mathbb{O} & \mathbb{O} & \mathbb{O} & \mathbb{B} & \mathbb{C}_{32} + \mathbb{C}_\gamma \end{bmatrix}. \tag{12}$$

This is a convenient choice because, to compute the residual at each iteration of a Krylov method, each block of (12) can be considered as an independent mono-compartment Darcy problem which can be solved using an internal GMRES method and applying the aSIMPLE preconditioner adapted to the Darcy case. As for the external iterations, we consider the Flexible-GMRES (FGMRES) variant of GMRES to deal with the fact that at each iteration we are solving each subproblem inexactly, up to a prescribed tolerance [58].

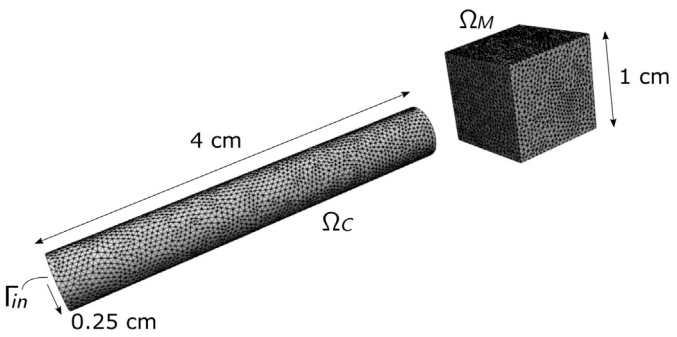


Fig. 7. Computational meshes of domains Ω_C and Ω_M. Test I.

Table 1
Estimated parameters of the coupled problem. Test I.

$\beta_{1,2}$ $[(\text{Pa}\cdot\text{s})^{-1}]$	$\beta_{2,3}$ $[(\text{Pa}\cdot\text{s})^{-1}]$	α $[\text{cm}^3\cdot(\text{Pa}\cdot\text{s})^{-1}]$	K_1 $[\text{cm}^2\cdot(\text{Pa}\cdot\text{s})^{-1}]$	K_2 $[\text{cm}^2\cdot(\text{Pa}\cdot\text{s})^{-1}]$
$2.60\cdot10^{-6}$	$3.62\cdot10^{-6}$	$2.98\cdot10^{-6}$	$5.85\cdot10^{-5}$	$8.40\cdot10^{-6}$

4. Numerical results

In this section, we present several numerical results aiming at assessing the reliability, stability and accuracy of the proposed methods and algorithms. In particular, we consider a first test in an ideal domain to check the validity of the code (Test I) and a second one in a real computational domain of human coronaries and myocardial ventricles to test the robustness and validity of the method when operating on physiological data (Test II). At the end, we present an application of the model to a patient-specific case to provide a preliminary comparison between the results and measured clinical data (Test III).

In all the numerical simulations of the coupled problem given by iterations (7)-(8) in Algorithm 2, we used the following parameters: $\rho = 1.06$ g/cm^3, $\mu = 0.035$ dyne/cm^2, $\gamma = 10^{-4}\,1/(\text{Pa}\cdot\text{s})$, $N_{iso-epi} = 3$, $N_{iso} = 300$, $\Delta t = 0.01$ s, $\varepsilon_{tol} = 10^{-5}$, the scalar permeability K_3 is chosen equal to 10^{-3} cm$^2\cdot(\text{Pa}\cdot\text{s})^{-1}$ according to [35], whereas the scalar permeabilities K_1 and K_2 are estimated as described in Section 2.4.3. We consider in all the cases three Darcy compartments and we set $p_{veins} = 22.5$ mmHg [47].

In order to ensure that blood flow reaches the myocardium despite using a rigid model of the heart, we prescribe at the inlet of the 3D coronaries a Dirichlet boundary condition for the 3D NS. Such condition enforces a flow rate that is mainly active during the diastole, as expected in the physiological conditions. Such model input partially compensates the absence of heart contraction.

All the numerical simulations of the coupled problem (3) are performed using the FE library LifeV (https://bitbucket.org/lifev-dev/lifev-release/wiki/Home). The numerical simulations of both the eikonal problem (4) and the Laplace equation (5) are instead obtained using a numerical solver implemented in FEniCS [3,44].

4.1. Test I: idealized geometry

In the first numerical test, we consider the computational domain given by an idealized cylindrical coronary Ω_C and by a cube Ω_M representing a portion of the myocardium, see Fig. 7.

At the inlet section Γ_{in} of the coronary vessel, we prescribe the following flow rate condition:

$$\rho \int_{\Gamma_{in}} \boldsymbol{u}_C \cdot \boldsymbol{n} d\gamma = Q_{in},$$

where $Q_{in}(t) = q_{Poiseuille} sin(2\pi t)$ cm^3/s for $t \leq 0.5$ s and null elsewhere, and $q_{Poiseuille}$ is the flow rate at the inlet of the intramural vascular network obtained by the Poiseuille flow model. In particular, we obtain $q_{Poiseuille} = 8.68\cdot10^{-3}$ cm^3/s.

In this test we want to check the mass conservation in the implementation of Algorithm 2 and the performance of Algorithm 1. To this aim, we build a network in Ω_M with Algorithm 1, we solve the coupled problem with Algorithm 2, and we compare the average pressure gradient between the first and the second compartments with the average pressure gradient obtained by the Poiseuille flow model used to estimate the parameters of the model. The intramural network is shown in Fig. 8 and the estimation of the parameters of the coupled problem leads the values reported in Table 1.

In Fig. 9a we show the results of the simulation for $t = 0.25s$ (peak value of inlet velocity). We observe a pressure gradient going from the domain Ω_C to the domain Ω_M, according to the direction of the flow imposed at the inlet surface.

In Fig. 9b we report the inlet flow rate Q_{in} and the outlet flow rate $Q_{out} = \gamma(p_{M,3} - p_{veins})$. We notice that the two profiles are in excellent agreement, so we can conclude that the mass conservation is respected.

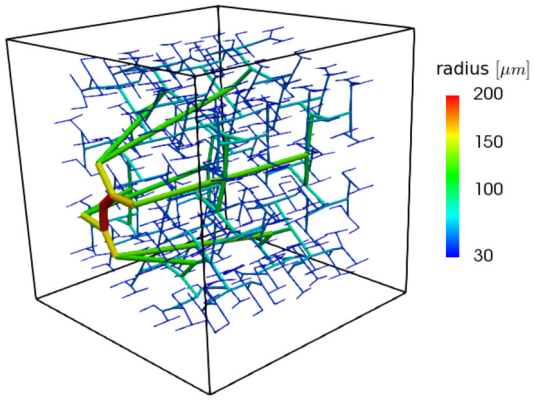


Fig. 8. Intramural network generated inside the domain Ω_M (the cylinder Ω_C is on the left). Test I.

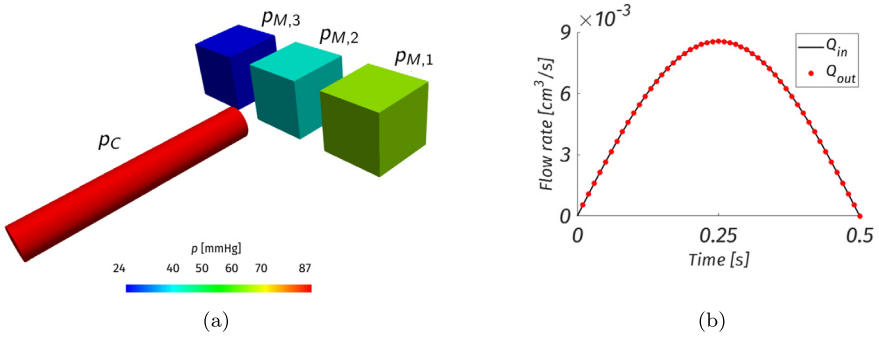


Fig. 9. (a) Pressure solution at the peak value of inlet flow rate ($t = 0.25$) (the legend is the same for $p_C, p_{M,1}, p_{M,2}, p_{M,3}$); (b) inlet flow rate Q_{in} and the outlet flow rate Q_{out}. Test I.

Table 2
Jump of average-in-space pressures between compartments 1 and 2 estimated by the Poiseuille solution and in the multi-compartment Darcy model ($t = 0.25$). Test I.

	ΔP_{12} [mmHg]
Poiseuille	25.02
multi-compartment Darcy	24.66

Finally, the jump of the average-in-space pressure obtained by the Poiseuille solution between inlet and outlet of the intramural vessels and computed using (6) is compared in Table 2 with the jump of average-in-space pressures between the first and the second compartments in the multi-compartment Darcy model. The difference is about 1.4%. We conclude that the estimation of the parameters in the multi-compartment Darcy model, which is based only on the first and second compartments, is consistent and accurate.

4.2. Test II: realistic geometry

4.2.1. Simulation set up and parameter estimation

In the second numerical test, we apply the proposed multi-physics computational model to a realistic 3D human heart geometry. To this purpose the geometries of the computational domains Ω_C and Ω_M, describing the arterial epicardial vessels and the myocardium of the left and right ventricles are defined starting from the 3D Human Heart Model provided by Zygote [1] (see Fig. 10). We remark that similar input data for the morphology of both the ventricles and the coronaries could be reconstructed by clinical data, for example CTA. The corresponding computational meshes are composed by 417,969 tetrahedral elements for Ω_C and 365,142 tetrahedral elements for Ω_M.

Following the procedure described in Sect. 2.4.1, we performed the partitioning of the domain Ω_M and we obtained 17 perfusion regions, starting from 17 outflow sections. The results are shown in Fig. 11.

The surrogate intramural network generated by means of Algorithm 1 inside these perfusion regions is composed by 71,179 vessels (see Fig. 12) and the parameter estimated by using this network is shown in Fig. 13. Its morphology seems very similar to a coronary network, see for example the network generated in [65]. Notice that in this figure, for vi-

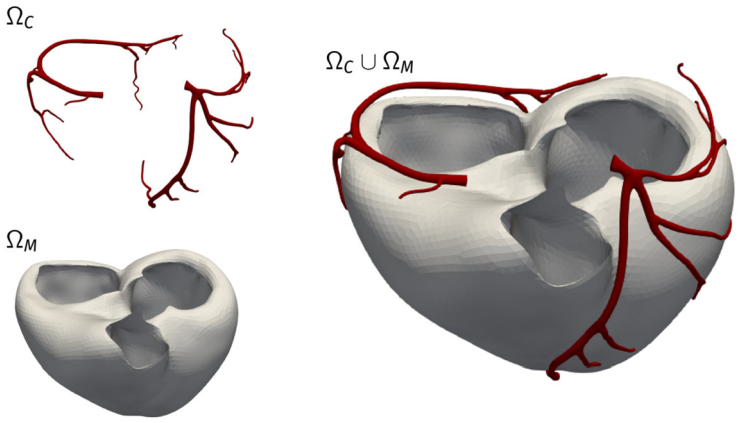


Fig. 10. Computational domains Ω_C and Ω_M. Test II.

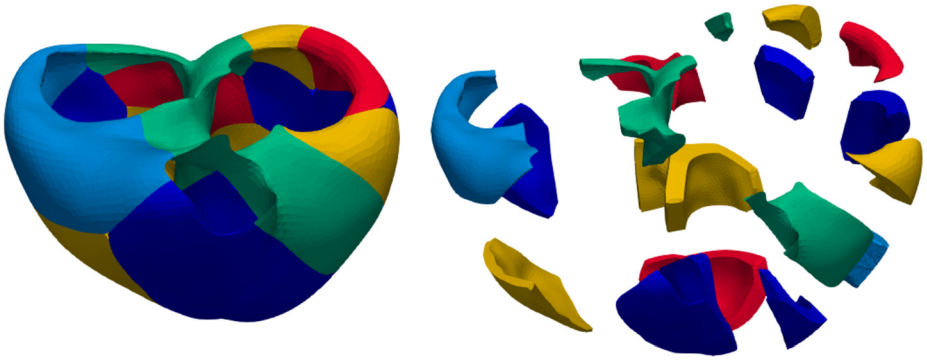


Fig. 11. Perfusion regions obtained in the domain Ω_M. Test II.

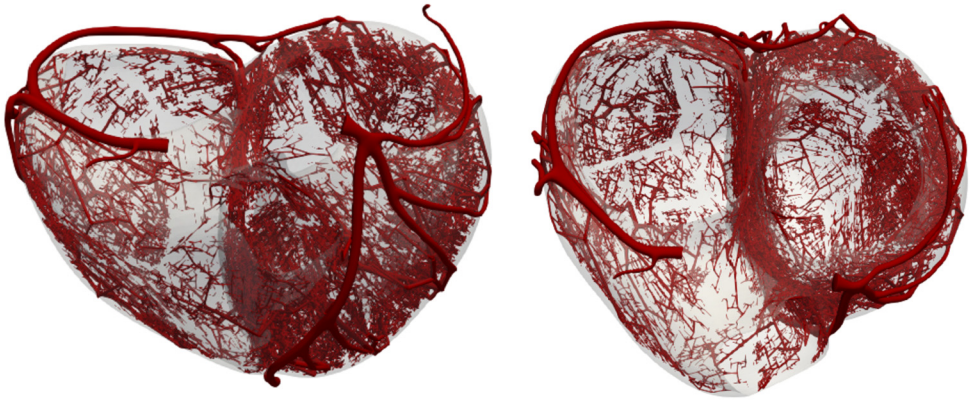


Fig. 12. Intramural vascular network generated inside the domain Ω_M. Test II.

sualization purposes, we have plotted the global conductance function $\alpha = \sum_j \alpha^j \chi_{\Omega_M^j}$ and the global porosity function $\phi = \sum_{i=1}^{3} \sum_j \phi_i^j \chi_{\Omega_M^j}$ obtained as sum over the three compartments.

Introducing the average-in-space porosity $\overline{\phi_M} = \sum_{i=1}^{N} \overline{\phi_i}$, $\overline{\phi_i} = \sum_{j=1}^{J} \phi_i^j V_{\Omega_M^j} / V_{\Omega_M}$, from these results we obtain $\overline{\phi_M} = 0.095$, a value in accordance with the literature [35].

At the inlet sections $\Gamma_{in,\beta}$, with $\beta = l, r$, of the epicardial vessels, we prescribe the following flow rate condition:

$$\rho \int_{\Gamma_{in,\beta}} \boldsymbol{u}_C \cdot \boldsymbol{n} d\gamma = Q_{in,\beta}, \ \beta = l, r,$$

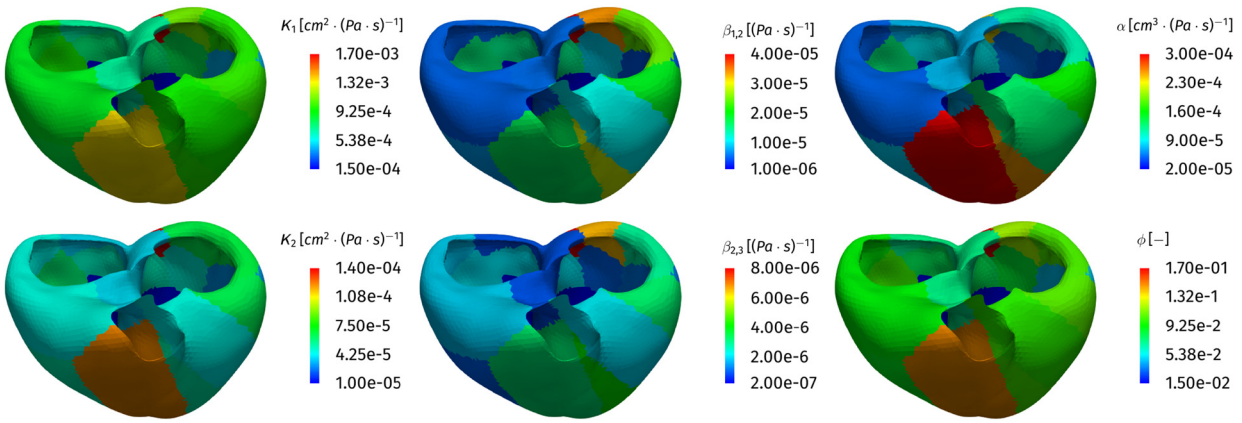


Fig. 13. Parameters estimated inside Ω_M. Test II.

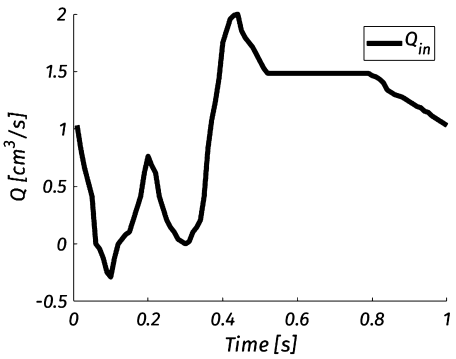


Fig. 14. Total physiological inlet coronary flow rate. Test II.

where $Q_{in,l} = 0.57Q_{in}$, $Q_{in,r} = 0.43Q_{in}$ and Q_{in} being the inlet coronary flow rate with a physiological profile shown in Fig. 14 [52]. The subdivision of Q_{in} in $Q_{in,l}$ and $Q_{in,r}$ accounts for percentage of volume perfused by each branch.

4.2.2. Comparison between implicit and explicit strategies for Algorithm 2

The aim of this section is twofold. First, we want to investigate whether the explicit version of Algorithm 2 (obtained by performing just 1 iteration per time step) is usable for applications, i.e. if it is stable and accurate with respect to the implicit version. Secondly, we want to quantify the convergence properties of the implicit version, i.e. the average number of iterations needed to converge.

Regarding the first aim, we first notice that the explicit version of Algorithm 2 is stable and produces meaningful results. Moreover, in Fig. 15 we plot for three different time steps the coronary pressure p_C and an average (over the three compartments) myocardial pressure p_M, defined as follows:

$$p_M = \frac{\sum_{i=1}^{3} \overline{\phi_i} p_{M,i}}{\overline{\phi_M}},$$

where $\overline{\phi_i}$ and $\overline{\phi_M}$ are the average porosities defined above.

We notice an excellent agreement between the solutions obtained by the two strategies, apart from the systole in the coronaries, where slight differences could be noticed which however disappear in the following instants.

To better evaluate the differences between implicit and the explicit strategies (that is the error of the explicit strategy with respect to the implicit one), we compute at each time step the relative differences $diff_{p_C}$ and $diff_{p_M}$ in the L^2 norms for the pressure solutions, see Fig. 16. Regarding the coronary pressure, the error is bigger in the first half of the heartbeat (mean percentage equal to 8.4%) where the flow rate experiences significant variations, whereas it is quite negligible in the second half of the period (mean percentage equal to 0.47%). Instead, for the myocardial pressure the error is always negligible, being at most equal to 0.05%.

In Fig. 17 we report the number of iterations needed by the implicit iterative strategy. We observe that the number of iterations strongly depends on the instant of the heartbeat: during the first part of the heart cycle, when the flow features large variations, the number of iterations is quite high, up to 7, whereas in the second part, when the flow is almost

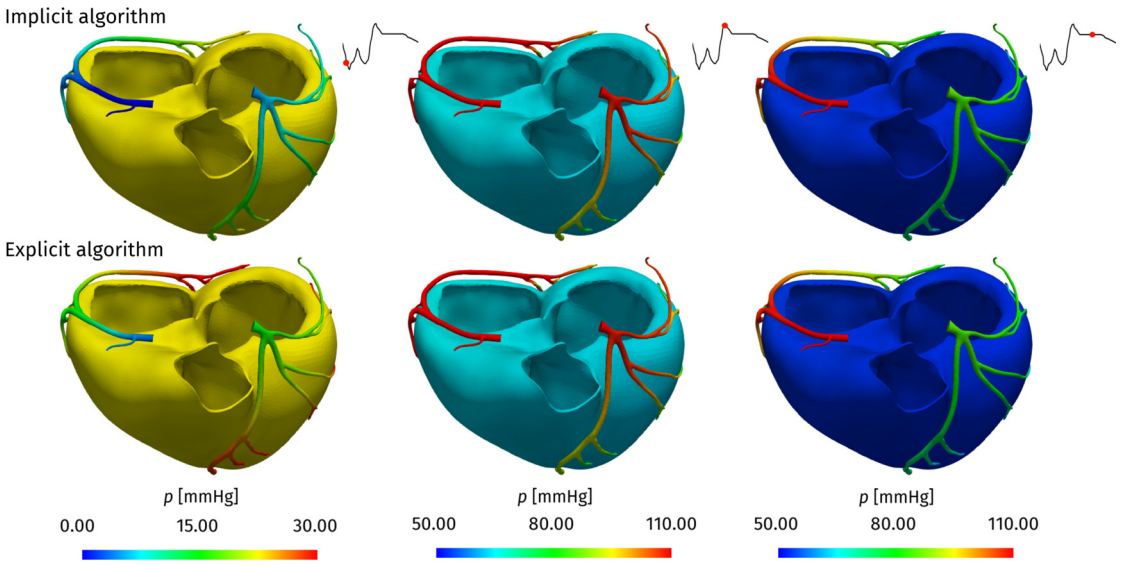


Fig. 15. Pressure field for $t = 0.06$, $t = 0.44$ and $t = 0.70$ (the legend is the same for p_C and p_M). Test II.

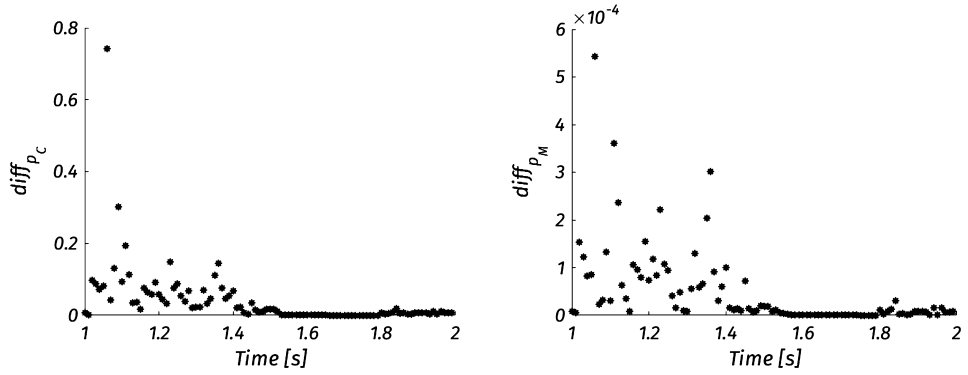


Fig. 16. Relative differences in L^2 norm between explicit and implicit strategies of Algorithm 2. Left: coronary pressure; Right: myocardial pressure. Test II.

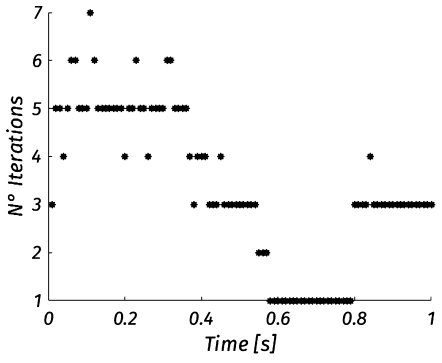


Fig. 17. Number of iterations needed by the implicit strategy to reach convergence. Test II.

constant, the number of iterations significantly decreases (average along all the heartbeat equal to 3.3 iterations). This is in accordance with the trend of the explicit algorithm error discussed above.

We conclude that the explicit version of Algorithm 2 is an effective alternative to the implicit one since it allows to reduce the computational effort (1 vs 3.3 iterations per time step). However, it produces an error for the coronary pressure which could be significant for some applications (average error 4% along all the heartbeat). Thus, if one needs a better accuracy, then the implicit method should be preferred.

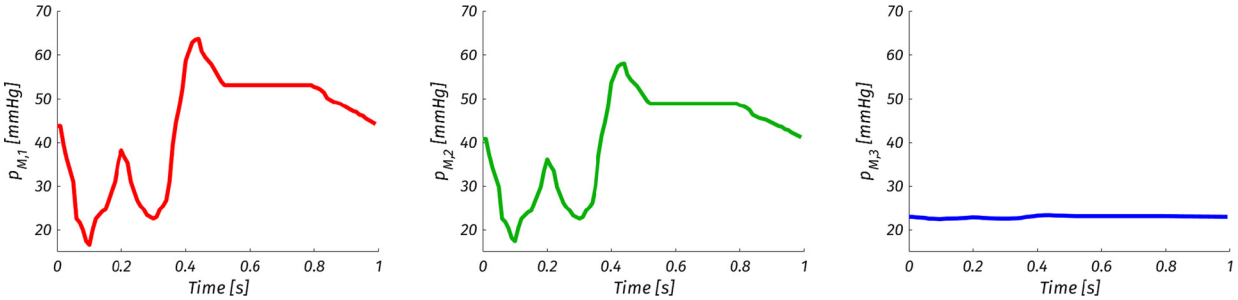


Fig. 18. Average-in-space pressure in the three compartments of the multi-compartment Darcy model. Left: $p_{M,1}$; Middle: $p_{M,2}$; Right: $p_{M,3}$. Test II.

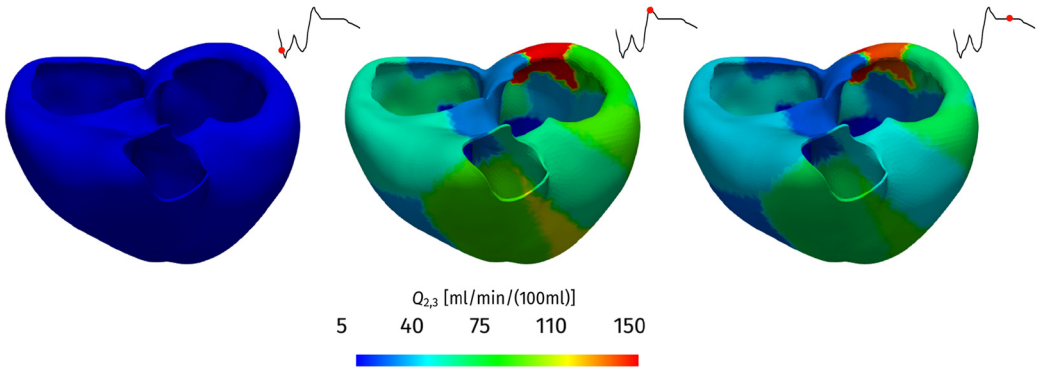


Fig. 19. Perfusion rate into the third compartment at $t = 0.06$ s, $t = 0.44$ s and $t = 0.70$ s. Test II.

4.2.3. Analysis of the pressure and flow fields

We discuss in what follows the physiological significance of the results. We refer to the implicit solution since from the accuracy point of view is our gold-standard.

From Fig. 15 we notice that the pressure in both Ω_C and Ω_M is in the physiological range. This is also highlighted by Fig. 18 where we plot the average-in-space pressure profiles in the three compartments of the multi-compartment Darcy model. Notice also that, unlike the first and the second compartments, in the third compartment the pressure profile is subject to a damping effect due to the sink term. This is consistent with the loss of pulsatility inside the capillary vessels.

In Fig. 19 we plot the flow rate entering in the third compartment, normalized over 100 ml of tissue. This is the amount of blood entering in the myocardial tissue, which is computed as:

$$Q_{2,3} = \beta_{2,3}(p_{M,2} - p_{M,3}) * 60 \text{ s/min} * 100 \text{ ml},$$

where the factor 60 s/min is used to express the perfusion rate in minutes. From these results, it is possible to notice an heterogeneous distribution of perfusion rate inside the domain Ω_M due to the heterogeneity of the parameters and consequently to the different resistance of the vessels inside each perfusion region.

Computing an average-in-space perfusion rate at $t = 0.44$ s (when the inlet velocity is maximum in time), we obtain about 62 ml/min/100 ml, which is less than the physiological perfusion rate which is about 130 ml/min/100 ml [46]. However, locally, our model is able to recover physiological values (see Fig. 19). We believe that this discrepancy can be mitigated when we will extend model of the coronary tree with the action of transversal branches and the corresponding outlets. Indeed, this improvement of the model will allow to increase the inlet flow rate and accordingly the average perfusion rate. With a more detailed coronary reconstruction and including transversal vessels, it will be also possible to obtain more homogeneous parameters for the multi-compartment Darcy model and significant values of perfusion in all the myocardium. This issue is under study for future investigations.

4.3. Test III: preliminary comparison with clinical data

We present here a very preliminary result about the comparison of the perfusion obtained with the proposed model and a Myocardial Blood Flow (MBF) map of an healthy person obtained by stress myocardial computed tomography perfusion (stress-CTP) at Centro Cardiologico Monzino, Milan, Italy. STRESS-CTP is an effective strategy to perform the diagnosis of coronary artery disease [22,50] and allows to measure the myocardial perfusion highlighting the regions scarcely perfused.

The reconstruction of the geometry has been performed by means of VMTK [4] and MITK (http://www.mitk.org/wiki/MITK) starting from CTA, and a computational mesh has been built with the novel semi-automatic meshing tool proposed

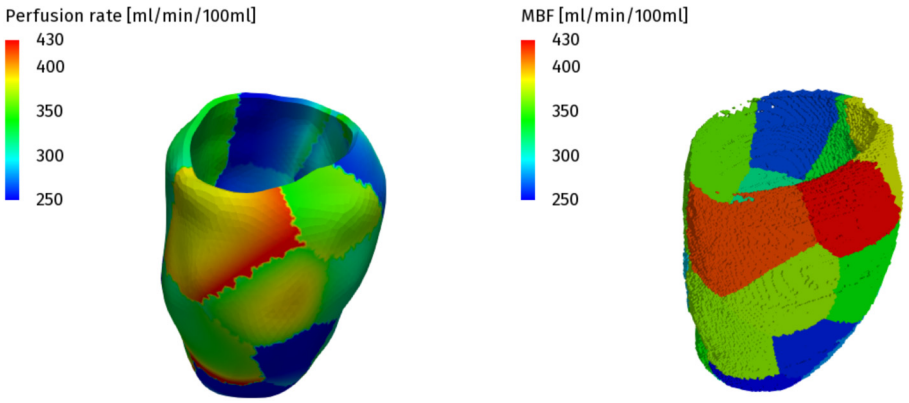


Fig. 20. Comparison between perfusion rate at the peak instant in the third compartment computed by the model (left) and MBF measured by STRESS-CTP (right). Test III.

in [24]. The same computational parameters and settings of test II have been considered, apart from an increased value of the input flow rate (5 times the one used in test II) to account for the stress conditions, the time step which was $\Delta t = 0.001$ s and an augmented value of $\beta_{2,3}$ in the septum to compensate a lack of reconstructed coronaries in this region due to insufficient image resolution.

In Fig. 20 we show a comparison between computed perfusion rate and measured MBF at the peak instant. For the latter, we plotted the average value in each computed perfusion region. We observe a very good general agreement between the two distributions. In particular, some perfusion regions are well predicted in terms of perfusion by our model, whereas in other ones the computational model underestimated the measured perfusion. A more extensive set of test cases about the feasibility of the proposed mathematical framework is currently under examination in order to move towards a validation of our proposed model.

5. Conclusions, limitations and perspectives

We developed a multi-physics model for the cardiac perfusion. This is based on coupling the 3D Navier-Stokes equations for the epicardial coronaries and a multi-compartment Darcy model for the intramural vessels. To estimate the parameters in the latter model, we proposed an algorithm to generate an intramural vascular network starting from the epicardial coronaries. We also addressed the numerical solution of this coupled problem, by proposing a splitting algorithm and a suitable preconditioner for the multi-compartment Darcy model. The application of our framework to a realistic human heart including both the ventricles leads to accurate results for the pressures and for the local perfusion rate, which agreed with the physiological values. An advantage of the proposed model is that it can be set up using only *in-vivo* clinical images, such as a CT scan of heart, in particular CT angiography. Indeed, the geometry of both epicardial coronaries and ventricles can be reconstructed from this kind of medical images. Conversely, for the best of our knowledge, more accurate multi-compartment perfusion models, previously proposed in [41,35,15,42], need detailed information on microvascular structure that is only available from *ex-vivo* data.

Several limitations affect the present study.

First, we are aware that a mismatch between the anatomical and physiological assessments is unavoidable [6] and that it is necessary to impose physiological flow constraints to the whole network to ensure realistic geometric reconstruction [49].

Second, we neglected the heart movement, despite the well know dynamic myocardium-vessel interaction. This is a significant limitation since changes of resistances in the intramural vessels due to the heart contraction and relaxation affect the perfusion rate. To overcome this limitation, we have prescribed the flow rate at the coronary inflow. The inclusion of the heart movement by means of a multi-compartment poro-mechanics model is under investigation. This extension of the model should allow us to prescribe the pressure at the coronary inflow and the right perfusion rate should be obtained directly by the model.

A third limitation consists in the absence of transversal vessels arising from the main coronaries. The inclusion of such vessels should allow us to obtain more homogeneous parameters for the multi-compartment Darcy model and a more uniform perfusion for the healthy case. This limit was partially compensated by our inclusion of all vessels, including the smallest capillaries, by means of the Darcy model based on the fact that the blood flow in the myocardium is supplied in outside-in fashion, from the large epicardial coronary arteries to the myocardial and endocardial vessels [29].

Finally, we mention the absence of any anatomical and physiological criteria in the intramural network generation algorithm. In this first work, for the sake of simplicity, we preferred to use a pure geometric criterion to determine the angle, based on the barycenter of subvolumes and the Murray law. However, the use of anatomical and physiological criteria

to generate the network would represent an important step to improve the results. The inclusion of such criteria in our framework is currently under study.

Declaration of competing interest

The authors declare that they have no known competing financial interests or personal relationships that could have appeared to influence the work reported in this paper.

Acknowledgements

This project has received funding from the European Research Council (ERC) under the European Union's Horizon 2020 research and innovation programme (grant agreement No. 740132, iHEART - An Integrated Heart Model for the simulation of the cardiac function, P.I. Prof. A. Quarteroni).

References

[1] Zygote solid 3d heart generation ii development report, Technical report, Zygote Media Group Inc., 2014.
[2] P. Agger, S. Lakshminrusimha, C. Laustsen, S. Gugino, J.R. Frandsen, M. Smerup, R.H. Anderson, V. Hjortdal, R.H. Steinhorn, The myocardial architecture changes in persistent pulmonary hypertension of the newborn in an ovine animal model, Pediatr. Res. 79 (4) (apr 2016) 565–574.
[3] M.S. Alnæs, J. Blechta, J. Hake, A. Johansson, B. Kehlet, A. Logg, C. Richardson, J. Ring, M.E. Rognes, G.N. Wells, The fenics project version 1.5, Arch. Numer. Softw. 3 (100) (2015).
[4] L. Antiga, M. Piccinelli, L. Botti, B. Ene-Iordache, A. Remuzzi, D.A. Steinman, An image-based modeling framework for patient-specific computational hemodynamics, Med. Biol. Eng. Comput. 46 (11) (2008) 1097.
[5] S. Badia, F. Nobile, C. Vergara, Fluid-structure partitioned procedures based on Robin transmission conditions, J. Comput. Phys. 227 (2008) 7027–7051.
[6] Y.G. Bae, S.T. Hwang, H. Han, S.M. Kim, H. Kim, I. Park, J.M. Lee, Y. Moon, J. Choi, Non-invasive coronary physiology based on computational analysis of intracoronary transluminal attenuation gradient, Sci. Rep. 8 (1) (2018) 4692.
[7] J.D. Bayer, R.C. Blake, G. Plank, N.A. Trayanova, A novel rule-based algorithm for assigning myocardial fiber orientation to computational heart models, Ann. Biomed. Eng. 40 (10) (Oct 2012) 2243–2254.
[8] L. Berger, R. Bordas, K. Burrowes, V. Grau, S. Tavener, D. Kay, A poroelastic model coupled to a fluid network with applications in lung modelling, Int. J. Numer. Methods Biomed. Eng. 32 (1) (2016) e02731.
[9] P.J. Blanco, R.A.B. de Queiroz, R.A. Feijóo, A computational approach to generate concurrent arterial networks in vascular territories, Int. J. Numer. Methods Biomed. Eng. 29 (5) (may 2013) 601–614.
[10] P.J. Blanco, R.A. Feijòo, S.A. Urquiza, A unified variational approach for coupling 3d-1d models and its blood flow applications, Comput. Methods Appl. Mech. Eng. 196 (2007) 4391–4410.
[11] P. Boettler, P. Claus, L. Herborts, M. McLaughlin, J. D'Hooge, B. Bijnens, S.Y. Ho, D. Kececioglu, G.R. Sutherland, New aspects of the ventricular septum and its function: an echocardiographic study, Heart 91 (10) (2005) 1343–1348.
[12] D. Caruso, M. Eid, U.J. Schoepf, K.N. Jin, A. Varga-Szemes, C. Tesche, S. Mangold, A. Spandorfer, A. Laghi, C.N. De Cecco, Dynamic CT myocardial perfusion imaging, Eur. J. Radiol. 85 (10) (2016) 1893–1899.
[13] D. Chapelle, J.F. Gerbeau, J. Sainte-Marie, I.E. Vignon-Clementel, A poroelastic model valid in large strains with applications to perfusion in cardiac modeling, Comput. Mech. 46 (1) (2010) 91–101.
[14] W.M. Chilian, S.M. Layne, E.C. Klausner, C.L. Eastham, M.L. Marcus, Redistribution of coronary microvascular resistance produced by dipyridamole, Am. J. Physiol., Heart Circ. Physiol. 256 (2) (1989) 25/2.
[15] A.N. Cookson, J. Lee, C. Michler, R. Chabiniok, E. Hyde, D.A. Nordsletten, M. Sinclair, M. Siebes, N.P. Smith, A novel porous mechanical framework for modelling the interaction between coronary perfusion and myocardial mechanics, J. Biomech. 45 (5) (2012) 850–855.
[16] C. Dapogny, P. Frey, Computation of the signed distance function to a discrete contour on adapted triangulation, Calcolo 49 (3) (jan 2012) 193–219.
[17] C. Daviller, T. Grenier, H. Ratiney, M. Sdika, P. Croisille, M. Viallon, Automatic myocardial ischemic lesion detection on magnetic resonance perfusion weighted imaging prior perfusion quantification: a pre-modeling strategy, Comput. Biol. Med. 110 (April 2019) 108–119.
[18] S. Deparis, M. Discacciati, G. Fourestey, A. Quarteroni, Fluid-structure algorithms based on Steklov-Poincaré operators, Comput. Methods Appl. Mech. Eng. 195 (41–43) (2006) 5797–5812.
[19] S. Deparis, G. Grandperrin, A. Quarteroni, Parallel preconditioners for the unsteady Navier-Stokes equations and applications to hemodynamics simulations, Comput. Fluids 92 (2014) 253–273.
[20] M. Discacciati, A. Quarteroni, A. Valli, Robin–Robin domain decomposition methods for the Stokes–Darcy coupling, SIAM J. Numer. Anal. 45 (3) (2007) 1246–1268.
[21] R. Doste, D. Soto-Iglesias, G. Bernardino, A. Alcaine, R. Sebastian, S. Giffard-Roisin, M. Sermesant, A. Berruezo, D. Sanchez-Quintana, O. Camara, A rule-based method to model myocardial fiber orientation in cardiac biventricular geometries with outflow tracts, Int. J. Numer. Methods Biomed. Eng. 35 (4) (2019).
[22] B.L. Eck, R. Fahmi, J. Levi, A. Fares, H. Wu, Y. Li, M. Vembar, A. Dhanantwari, H.G. Bezerra, D.L. Wilson, Comparison of quantitative myocardial perfusion imaging ct to fluorescent microsphere-based flow from high-resolution cryo-images, in: Proc SPIE Int Soc Opt Eng, 2016, p. 9788, 97882F.
[23] R.N. Elias, M.A.D. Martins, A.L.G.A. Coutinho, Simple finite element-based computation of distance functions in unstructured grids, Int. J. Numer. Methods Eng. 72 (9) (2007) 1095–1110.
[24] M. Fedele, Polygonal surface processing and mesh generation tools for numerical simulations of the complete cardiac function, MOX Report 32, Politecnico di Milano, 2019.
[25] M. Fedele, E. Faggiano, L. Dedè, A. Quarteroni, A patient-specific aortic valve model based on moving resistive immersed implicit surfaces, Biomech. Model. Mechanobiol. 16 (5) (2017) 1779–1803.
[26] L. Formaggia, C. Vergara, Prescription of general defective boundary conditions in fluid-dynamics, Milan J. Math. 80 (2) (2012) 333–350.
[27] D. Forti, L. Dedè, Semi-implicit BDF time discretization of the Navier–Stokes equations with VMS-LES modeling in a high performance computing framework, Comput. Fluids 117 (2015) 168–182.
[28] A. Gonzalez-Tendero, C. Zhang, V. Balicevic, R. Cardenes, S. Loncaric, C. Butakoff, B. Paun, A. Bonnin, P. Garcia-Cañadilla, E. Muñoz-Moreno, E. Gratacos, F. Crispi, B. Bijnens, Whole heart detailed and quantitative anatomy, myofiber structure and vasculature from X-ray phase-contrast synchrotron radiation-basedmicro computed tomography, Eur. Heart J. Card. Imaging 18 (7) (2017) 732–741.
[29] A.G. Goodwill, G.M. Dick, A.M. Kiel, J.D. Tune, Regulation of Coronary Blood Flow, American Cancer Society, 2017, pp. 321–382.

[30] B. Guerciotti, C. Vergara, S. Ippolito, A. Quarteroni, C. Antona, R. Scrofani, A computational fluid-structure interaction analysis of coronary Y-grafts, Med. Eng. Phys. 47 (2017) 117–127.
[31] H. Zhao, A fast sweeping method for Eikonal equations, Math. Comput. 74 (250) (may 2004) 603–628.
[32] J.M. Huyghe, Finite deformation theory of hierarchically arranged porous solids (Constitutive behaviour), Int. J. Eng. Sci. 33 (13) (1995) 1873–1886.
[33] J.M. Huyghe, D.H. Van Campen, Finite deformation theory of hierarchically arranged porous solids-I. Balance of mass and momentum, Int. J. Eng. Sci. 33 (13) (1995) 1861–1871.
[34] E.R. Hyde, C. Michler, J. Lee, A.N. Cookson, R. Chabiniok, D.A. Nordsletten, N.P. Smith, Parameterisation of multi-scale continuum perfusion models from discrete vascular networks, Med. Biol. Eng. Comput. 51 (5) (2013) 557–570.
[35] E.R. Hyde, A.N. Cookson, J. Lee, C. Michler, A. Goyal, T. Sochi, R. Chabiniok, M. Sinclair, D.A. Nordsletten, J. Spaan, J.P.H.M. Van Den Wijngaard, M. Siebes, N.P. Smith, Multi-scale parameterisation of a myocardial perfusion model using whole-organ arterial networks, Ann. Biomed. Eng. 42 (4) (2014) 797–811.
[36] C. Jaquet, L. Najman, H. Talbot, L. Grady, M. Schaap, B. Spain, H.J. Kim, I. Vignon-Clementel, C.A. Taylor, Generation of patient-specific cardiac vascular networks: a hybrid image-based and synthetic geometric model, IEEE Trans. Biomed. Eng. 66 (4) (2019) 946–955.
[37] F. Kabinejadian, D.N. Ghista, Compliant model of a coupled sequential coronary arterial bypass graft: effects of vessel wall elasticity and non-Newtonian rheology on blood flow regime and hemodynamic parameters distribution, Med. Eng. Phys. 34 (7) (2012) 860–872.
[38] B. Kaimovitz, Y. Lanir, G.S. Kassab, Large-scale 3-d geometric reconstruction of the porcine coronary arterial vasculature based on detailed anatomical data, Ann. Biomed. Eng. 33 (11) (nov 2005) 1517–1535.
[39] G.S. Kassab, C.A. Rider, N.J. Tang, Y.C. Fung, Morphometry of pig coronary arterial trees, Am. J. Physiol., Heart Circ. Physiol. 265 (1) (1993) H350–H365.
[40] R. Kimmel, J.A. Sethian, Computing geodesic paths on manifolds, Proc. Natl. Acad. Sci. 95 (15) (jul 1998) 8431–8435.
[41] J. Lee, A. Cookson, R. Chabiniok, S. Rivolo, E. Hyde, M. Sinclair, C. Michler, T. Sochi, N. Smith, Multiscale modelling of cardiac perfusion, in: Modeling the Heart and the Circulatory System, Springer, 2015, pp. 51–96.
[42] J. Lee, D. Nordsletten, A. Cookson, S. Rivolo, N. Smith, In silico coronary wave intensity analysis: application of an integrated one-dimensional and poromechanical model of cardiac perfusion, Biomech. Model. Mechanobiol. 15 (6) (2016) 1535–1555.
[43] J. Lee, N.P. Smith, The multi-scale modelling of coronary blood flow, Ann. Biomed. Eng. 40 (11) (2012) 2399–2413.
[44] A. Logg, K.-A. Mardal, G.N. Wells, et al., Automated Solution of Differential Equations by the Finite Element Method, Springer, 2012.
[45] R.P. Marcus, K. Nikolaou, D. Theisen, M.F. Reiser, F. Bamberg, Myocardial perfusion imaging by computed tomography: today and tomorrow, Int. J. Clin. Pract. 65 (SUPPL. 173) (2011) 14–22.
[46] F.G. Meinel, U. Ebersberger, U.J. Schoepf, G.G. Lo, Y.H. Choe, Y. Wang, J.A. Maivelett, A.W. Krazinski, R.P. Marcus, F. Bamberg, C.N. De Cecco, Global quantification of left ventricular myocardial perfusion at dynamic CT: feasibility in a multicenter patient population, Am. J. Roentgenol. 2 (203) (2014) 174–180.
[47] C. Michler, A.N. Cookson, R. Chabiniok, E. Hyde, J. Lee, M. Sinclair, T. Sochi, A. Goyal, G. Vigueras, D.A. Nordsletten, N.P. Smith, A computationally efficient framework for the simulation of cardiac perfusion using a multi-compartment Darcy porous-media flow model, Int. J. Numer. Methods Biomed. Eng. 29 (2) (feb 2013) 217–232.
[48] A. Mishra, A. Jain, M. Hinduja, V. Wadhawa, R. Patel, N. Vaidhya, D. Rodricks, H. Patel, Transposition of great arteries with intramural coronary artery: experience with a modified surgical technique, Braz. J. Cardiovasc. Surg. 31 (1) (2016) 15–21.
[49] R. Namani, G.S. Kassab, Y. Lanir, Morphometric reconstruction of coronary vasculature incorporating uniformity of flow dispersion, Front. Physiol. 9 (2018) 1069.
[50] G. Pontone, D. Andreini, A.I. Guaricci, A. Baggiano, F. Fazzari, M. Guglielmo, G. Muscogiuri, C.M. Berzovini, A. Pasquini, S. Mushtaq, E. Conte, G. Calligaris, S. De Martini, C. Ferrari, S. Galli, L. Grancini, P. Ravagnani, G. Teruzzi, D. Trabattoni, F. Fabbiocchi, A. Lualdi, P. Montorsi, M.G. Rabbat, A.L. Bartorelli, M. Pepi, Incremental diagnostic value of stress computed tomography myocardial perfusion with whole-heart coverage ct scanner in intermediate- to high-risk symptomatic patients suspected of coronary artery disease, JACC: Cardiovasc. Imaging 12 (2) (feb 2019) 338–349.
[51] G. Pontone, M.G. Rabbat, A.I. Guaricci, Stress computed tomographic perfusion, Circ. Cardiovasc. Imaging 10 (4) (2017) 1–3.
[52] R. Ponzini, C. Vergara, A. Redaelli, A. Veneziani, Reliable CFD-based estimation of flow rate in haemodynamics measures, Ultrasound Med. Biol. 32 (10) (2006) 1545–1555.
[53] A. Porpora, P. Zunino, C. Vergara, M. Piccinelli, Numerical treatment of boundary conditions to replace lateral branches in haemodynamics, Int. J. Numer. Methods Biomed. Eng. 28 (12) (2012) 1165–1183.
[54] A. Quarteroni, L. Dede', A. Manzoni, C. Vergara, Mathematical Modelling of the Human Cardiovascular System: Data, Numerical Approximation, Clinical Applications, vol. 33, Cambridge University Press, 2019.
[55] A. Quarteroni, A. Manzoni, C. Vergara, The cardiovascular system: mathematical modelling, numerical algorithms and clinical applications, Acta Numer. 26 (2017) 365–590.
[56] A. Quarteroni, A. Valli, Domain Decomposition Methods for Partial Differential Equations, Oxford Science Publications, 1999.
[57] E. Rohan, V. Lukeš, A. Jonášová, Modeling of the contrast-enhanced perfusion test in liver based on the multi-compartment flow in porous media, J. Math. Biol. 77 (2) (2018) 421–454.
[58] Y. Saad, A flexible inner-outer preconditioned GMRES algorithm, SIAM J. Sci. Comput. 14 (2) (1993) 461–469.
[59] D. Sánchez-Quintana, M. Doblado-Calatrava, J.A. Cabrera, Y. Macías, F. Saremi, Anatomical basis for the cardiac interventional electrophysiologist, BioMed Res. Int. 2015 (2015) 1–24(Figure 1) .
[60] S. Sankaran, M. Esmaily Moghadam, A.M. Kahn, E.E. Tseng, J.M. Guccione, A.L. Marsden, Patient-specific multiscale modeling of blood flow for coronary artery bypass graft surgery, Ann. Biomed. Eng. 40 (10) (oct 2012) 2228–2242.
[61] M. Sankaranarayanan, D.N. Ghista, C.L. Poh, T.Y. Seng, G.S. Kassab, Analysis of blood flow in an out-of-plane CABG model, Am. J. Physiol., Heart Circ. Physiol. 291 (1) (2006) H283–H295.
[62] W. Schreiner, P.F. Buxbaum, Computer-optimization of vascular trees, IEEE Trans. Biomed. Eng. 40 (5) (may 1993) 482–491.
[63] W. Schreiner, R. Karch, M. Neumann, F. Neumann, P. Szawlowski, S. Roedler, Optimized arterial trees supplying hollow organs, Med. Eng. Phys. 28 (5) (2006) 416–429.
[64] N.P. Smith, A.J. Pullan, P.J. Hunter, An anatomically based model of transient coronary blood flow in the heart, SIAM J. Appl. Math. 62 (3) (jan 2002) 990–1018.
[65] Nicolas P. Smith, A.J. Pullan, P.J. Hunter, Generation of an anatomically based geometric coronary model, Ann. Biomed. Eng. 28 (1) (2000) 14–25.
[66] J. Spaan, C. Kolyva, J. Van Den Wijngaard, R. Ter Wee, P. Van Horssen, J. Piek, M. Siebes, Coronary structure and perfusion in health and disease, Philos. Trans. R. Soc. A, Math. Phys. Eng. Sci. 366 (1878) (2008) 3137–3153.
[67] J.A.E. Spaan, M. Siebes, R. ter Wee, C. Kolyva, J.W.G.E. van Teeffelen, H. Vink, D.S. Fokkema, G. Streekstra, E. VanBavel, Visualisation of intramural coronary vasculature by an imaging cryomicrotome suggests compartmentalisation of myocardial perfusion areas, Med. Biol. Eng. Comput. 43 (4) (2005) 431–435.
[68] C.D. Steadman, M. Jerosch-Herold, B. Grundy, S. Rafelt, L.L. Ng, I.B. Squire, N.J. Samani, G.P. McCann, Determinants and functional significance of myocardial perfusion reserve in severe aortic stenosis, JACC: Cardiovasc. Imaging 5 (2) (2012) 182–189.
[69] M. Howatson Tawhai, A.J. Pullan, P.J. Hunter, Generation of an anatomically based three-dimensional model of the conducting airways, Ann. Biomed. Eng. 28 (7) (2000) 793–802.

[70] T.E. Tezduyar, Stabilized Finite Element Formulations for Incompressible Flow Computations, Advances in Applied Mechanics, vol. 28, Elsevier, 1991, pp. 1–44.
[71] L. Thomas, T. Marwick, A.P. Bogdan, E. Donal, L.P. Badano, Left atrial structure and function, and left ventricular diastolic dysfunction: Jacc state-of-the-art review, J. Am. Coll. Cardiol. 73 (15) (2019) 1961–1977.
[72] L. Tobiska, G. Lube, A modified streamline diffusion method for solving the stationary Navier-Stokes equation, Numer. Math. 59 (1) (Dec 1991) 13–29.
[73] C. Vergara, Nitsche's method for defective boundary value problems in incompressible fluid-dynamics, J. Sci. Comput. 46 (1) (2011) 100–123.
[74] E. Vidotto, T. Koch, T. Köppl, R. Helmig, B. Wohlmuth, Hybrid models for simulating blood flow in microvascular networks, Multiscale Model. Simul. 17 (3) (2018) 1076–1102.
[75] A.-T. Vuong, L. Yoshihara, W.A. Wall, A general approach for modeling interacting flow through porous media under finite deformations, Comput. Methods Appl. Mech. Eng. 283 (2015) 1240–1259.
[76] C.Y. Wang, James B. Bassingthwaighte, Area-filling distributive network model, Math. Comput. Model. 13 (10) (1990) 27–33.
[77] N. Westerhof, C. Boer, R.R. Lamberts, P. Sipkema, Cross-talk between cardiac muscle and coronary vasculature, Physiol. Rev. 86 (4) (2006) 1263–1308.
[78] Y. Yin, J. Choi, E.A. Hoffman, M.H. Tawhai, C.-L. Lin, A multiscale MDCT image-based breathing lung model with time-varying regional ventilation, J. Comput. Phys. 244 (jul 2013) 168–192.
[79] L. Yoshihara, C.J. Roth, W.A. Wall, Fluid-structure interaction including volumetric coupling with homogenised subdomains for modeling respiratory mechanics, Int. J. Numer. Methods Biomed. Eng. 33 (4) (jul 2016) e2812.
[80] M. Zamir, Optimality principles in arterial branching, J. Theor. Biol. 62 (1) (1976) 227–251.
[81] M. Zamir, Nonsymmetrical bifurcations in arterial branching, J. Gen. Physiol. 72 (6) (dec 1978) 837–845.
[82] M. Zamir, S. Phipps, B.L. Langille, T.H. Wonnacott, Branching characteristics of coronary arteries in rats, Can. J. Physiol. Pharm. 62 (12) (1984) 1453–1459.